Title

Optimization of Al2O3/TiO2/Al2O3 Multilayer Antireflection Coating With X-Ray Scattering Techniques

Permalink

https://escholarship.org/uc/item/5gx3r5t4

Author

Li, Chao

Publication Date

2018

Peer reviewed|Thesis/dissertation

UNIVERSITY OF CALIFORNIA

Los Angeles

Optimization of Al_2O_3/TiO_2/Al_2O_3 Multilayer Antireflection Coating

With X-Ray Scattering Techniques

A dissertation submitted in partial satisfaction

of the requirements for the degree Doctor of Philosophy

in Materials Science and Engineering

by

Chao Li

2018

ABSTRACT OF THE DISSERTATION

Optimization of Al_2O_3/TiO_2/Al_2O_3 Multilayer Antireflection Coating

With X-Ray Scattering Techniques

by

Chao Li

Doctor of Philosophy in Materials Science and Engineering

University of California, Los Angeles, 2018

Professor Mark S. Goorsky, Chair

Broadband multilayer antireflection coatings (ARCs) are keys to improving solar cell efficiencies. The goal of this dissertation is to optimize the multilayer Al_2O_3/TiO_2/Al_2O_3 ARC designed for a III-V space multi-junction solar cell with understanding influences of post-annealing and varying deposition parameters on the optical properties. Accurately measuring optical properties is important in accessing optical performances of ARCs. The multilayer Al_2O_3/TiO_2/Al_2O_3 ARC and individual Al_2O_3 and TiO_2 layers were characterized by a novel X-ray reflectivity (XRR) method and a combined method of grazing-incidence small angle X-ray scattering (GISAXS), atomic force microscopy (AFM), and XRR developed in this study. The novel XRR method combining an enhanced Fourier analysis with specular XRR simulation effectively determines layer thicknesses and surface and interface roughnesses and/or grading with sub-nanometer precision, and densities less than three percent uncertainty. Also, the combined method of

GISAXS, AFM, and XRR characterizes the distribution of pore size with one-nanometer uncertainty. Unique to this method, the diffuse scattering from surface and interface roughnesses is estimated with surface parameters (root mean square roughness σ, lateral correlation length ξ, and Hurst parameter h) obtained from AFM, and layer densities, surface grading and interface roughness/grading obtained from specular XRR. It is then separated from pore scattering. These X-ray scattering techniques obtained consistent results and were validated by other techniques including optical reflectance, spectroscopic ellipsometry (SE), glancing incidence X-ray diffraction, transmission electron microscopy and energy dispersive X-ray spectroscopy.

The ARCs were deposited by atomic layer deposition with standard parameters at 200 ℃. The as-deposited individual Al_2O_3 layer on Si is porous and amorphous as indicated by the combined methods of GISAXS, AFM, and XRR. Both post-annealing at 400 ℃ for 40 min in air and varying ALD parameters can eliminate pores, and lead to consistent increases in density and refractive index determined by the XRR method, SE, and optical reflectance measurements. After annealing, the layer remains amorphous. On the other hand, the as-deposited TiO_2 layer is non-porous and amorphous. It is densified and crystallized after annealing at 400 ℃ for 10 min in air. The multilayer $Al_2O_3/TiO_2/Al_2O_3$ ARC deposited on Si has surface and interface roughnesses and/or grading on the order of one nanometer. Annealing at 400 ℃ for 10 min in air induces densification and crystallization of the amorphous TiO_2 layer as well as possible chemical reactions between TiO_2 and Si diffusing from the substrate. On the other hand, Al_2O_3 layers remain amorphous after annealing. The thickness of the top Al_2O_3 layer decreases – likely due to interdiffusion between the top two layers and loss of hydrogen from hydroxyl groups

initially present in the ALD layers. The thickness of the bottom Al_2O_3 layer increases, probably due to the diffusion of Si atoms into the bottom layer. In addition, the multilayer Al_2O_3/TiO_2/Al_2O_3 ARC was deposited on AlInP (30nm) / GaInP (100nm) / GaAs that includes the topmost layers of III-V multi-junction solar cells. Reflectance below 5 % is achieved within nearly the whole wavelength range of the current-limiting sub-cell. Also, internal scattering occurs in the TiO_2 layer possibly associated with the initiated crystallization in the TiO_2 layer while absent in the amorphous Al_2O_3 layers.

The dissertation of Chao Li is approved.

Yu Huang

Diana L. Huffaker

Mark S. Goorsky, Committee Chair

University of California, Los Angeles

2018

Table of Contents

List of Figures

List of Tables

Acknowledgements

First of all, I would like to thank Professor Yu Huang, Professor Yang Yang, and Professor Diana Huffaker for serving on my committee and providing me valuable and insightful comments and suggestions. Particularly, my special thanks to my advisor, Professor Mark S. Goorsky. He is an excellent mentor enriching me with not only immense academic knowledge and skills, but also the rigorous academic attitude that I believe will benefit all my professional career.

I would like to thank the administrative staffs in the Department of Material Science and Engineering. They are always very kind and warm-hearted to help students get through various difficulties during the Ph.D. career. I would greatly appreciate the significant and valuable helps from my group members, Xiaolu, Jeff, Tingyu, Brett, Mark, Ariella, Sean, Steven, Michael, Eva, Pranav and many others, from the necessary experimental assists for my project to the supports and encouragements in many other aspects. The moment we share in our group would always be unforgettable. Also, I would like to thank Dr. Vincent Gambin and Dr. Randy Sandhu in Northrop Grumman for their help on MBE and Dr. Christopher Tassone in SLAC National Accelerator Laboratory and Mr. Phillip Kohl in Materials Research Laboratory at UCSB for their help on GISAXS measurements which are significant and indispensable for my project.

Finally, I would like to thank my parents. They always back me up that motivates me heading towards the destination of the Ph.D. journey. I couldn't imagine reaching the destination without their great and continued support and encouragement. Also, thanks to my girlfriend, Yuan Lin, for her essential help and understanding that make me through the hard and busy times.

VITA

2011   Bachelor of Science in Materials Science and Engineering

                Southeast University

                Nanjing, Jiangsu, China

2012   Master of Science in Materials Science and Engineering

                Carnegie Mellon University

                Pittsburgh, PA, USA

Publications

C. Li, F. Shahriarian, and M. S. Goorsky, "Grazing-Incidence Small Angle X-Ray Scattering, X-Ray Reflectivity, and Atomic Force Microscopy: A Combined Approach to Assess Atomic-Layer-Deposited Al_2O_3 Dielectric Films," J. Vac. Sci. Technol. A **36,** 01A115 (2018).

A. Aleman, C. Li, H. Zaid, H. Kindlund, J. Fankhauser, S. V. Prikhodko, M. S. Goorsky, and S. Kodambaka, "Ultra-High Vacuum Dc Magnetron Sputter-Deposition of Epitaxial Pd(111)/Al_2O_3(0001) Thin Films," Accepted by Journal of Vacuum Science and Technology A (2018).

W. Xin, I. M. De Rosa, P. Ye, J. Severino, C. Li, X. Yin, M. S. Goorsky, L. Carlson, and J. Yang, "Graphene Template Induced Growth of Single-crystalline Gold Nanobelts with High Structural Tunability," Nanoscale **10,** 2764 (2018).

J. Park, Y. S. Rim, C. Li, J. Wu, M. Goorsky, and D. Streit, "Defect-Induced Instability Mechanisms of Sputtered Amorphous Indium Tin Zinc Oxide Thin-Film Transistors" J. Appl. Phys. **123,** 161568 (2018).

H. Chen, Y. S. Rim, I. C. Wang, C. Li, B. Zhu, M. Sun, M. S. Goorsky, X. He, and Y. Yang, "Quasi-Two-Dimensional Metal Oxide Semiconductors Based Ultrasensitive Potentiometric Biosensors," ACS Nano **10,** A (2017).

W. Xin, J. Yang, C. Li, M. S. Goorsky, L. Carlson, and I. M. De Rosa, "Novel Strategy for One-Pot Synthesis of Gold Nanoplates on Carbon Nanotube Sheet As an Effective Flexible SERS Substrate," ACS Appl. Mater. Interfaces **9,** 6246 (2017).

J. Anaya, T. Bai, Y. Wang, C. Li, M. Goorsky, T. L. Bougher, L. Yates, Z. Cheng, S. Graham, K. D. Hobart, T. I. Feygelson, M. J. Tadjer, T. J. Anderson, B. B. Pate, and M. Kuball, "Simultaneous Determination of The Lattice Thermal Conductivity and Grain/Grain Thermal Resistance in Polycrystalline Diamond," Acta Mater. **139,** 215 (2017).

Z. Cheng, T. Bougher, T. Bai, Y. Wang, C. Li, L. Yates, B. M. Foley, M. Goorsky, B. A. Cola, and S. Graham, "Probing Growth-Induced Anisotropic Thermal Transport in CVD Diamond Membranes by Multi-frequency and Multi-spot-size Time-Domain Thermoreflectance," arXiv:1708.00405

M. S. Goorsky, T. Bai, C. Li, M. Tadjer, K. Hobart, T. J. Anderson, J. K. Hite, and B. N. Feigelson, "Novel Implantation Processing and Characterization for Scalable GaN Power Devices," ECS Trans. **80,** 251 (2017).

C. Li, F. Shahriarian, and M. S. Goorsky, "Determination of Atomic-Layer-Deposited Multilayer Antireflection Coating Parameters Using a Novel X-Ray Reflectivity Approach," ECS Trans. **75,** 155 (2016).

J. Park, Y. S. Rim, C. Li, H. Kim, M. Goorsky, and D. Streit, "Deep-Level Defect Distribution as a Function of Oxygen Partial Pressure in Sputtered ZnO Thin-Film Transistors," Curr. Appl. Phys. **16,** 1369 (2016).

C. Li, F. Shahriarian, and M. S. Goorsky, "The Characterization of Al_2O_3 and TiO_2 Antireflection Coatings with a Novel X-Ray Reflectivity Method and Other Experimental Techniques," Proc. 42th IEEE PVSC (2015).

Y. S. Rim, Y. (M) Yang, S. Bae, H. Chen, C. Li, M. S. Goorsky, and Y. Yang, "Ultrahigh and Broad Spectral Photodetectivity of an Organic–Inorganic Hybrid Phototransistor for Flexible Electronics," Adv. Mater. **27,** 6885 (2015).

Chapter 1 Introduction

1.1   Broadband Multilayer Antireflection Coating

1.1.1 Introduction to Multilayer Antireflection Coating

First initiated by Lord Rayleigh in the 19th century [1], antireflection coatings (ARCs) have been widely used in diverse applications such as eyeglasses [2], cameras [3], telescopes [4], and solar cells [5]. Specifically, innovations in solar cell technology pose an ever growing demand for minimization of light reflection on solar cell surfaces. Typically over 30 % of incident light throughout the UV/Vis/IR range is reflected on the solar cell surfaces due to the refractive index difference between solar cells and the ambient. This leads to loss of photons that would otherwise contribute to the overall efficiency. With refractive index values in between the refractive indices of solar cells and the ambient, ARCs enable to minimize the reflective loss through destructive interference of light reflected from ARC layers and solar cells.

Mathematically, based on Maxwell equations and interfacial continuity conditions, the normal reflectance R for an m-layer ARC can be calculated as [6],

$$R(N_m,\ldots,N_1,N_s,d_m,\ldots,d_1,\lambda) = r_{effm} r^*_{effm}$$

Eq. 1.1

where $N_j(\lambda) = n_j(\lambda) - ik_j(\lambda)$ and $N_s(\lambda) = n_s(\lambda) - ik_s(\lambda)$ are the refractive indices of Layer j and the substrate at the wavelength λ, d_j is the thickness of Layer j. r_{effm} is the effective reflection coefficient of the top (mth) layer. The effective reflection coefficient of Layer j, which is the amplitude ratio of the reflected wave to incident wave at the interface between Layer j+1 and Layer j, can be calculated as

$$r_{effj} = \frac{r_j + r_{effj-1}e^{-2i\delta_j}}{1 + r_j r_{effj-1}e^{-2i\delta_j}}$$

Eq. 1.2

where r_{effj-1} is the effective reflection coefficient of Layer j–1, r_j is the reflection coefficient at the interface between Layer j+1 and Layer j, and δ_j is the optical thickness of Layer j. r_j and δ_j can be calculated as

$$r_j = \frac{N_{j+1} - N_j}{N_{j+1} + N_j}$$

Eq. 1.3

$$\delta_j = \frac{2\pi}{\lambda} N_j d_j$$

Eq. 1.4

Starting from the bottom layer, r_{effm} can be calculated progressing to the top.

The optimal refractive index of Layer j can be determined by $n_j^2 = n_{j-1}n_{j+1}$, through which zero reflectance can be achieved at a target wavelength with optical thicknesses equal to ¼ of that wavelength. Figure 1.1 shows the calculated reflectance of ARCs with different number of layers for which the target wavelength is 550 nm near the peak of AM0 space solar spectrum. A substrate of AlInP (30 nm) / GaInP is used which is a simplification of III-V multi-junction solar cell structures including the topmost window layer AlInP (30 nm) and the GaInP top junction layer. As shown in Figure 1.1, the optical reflectance is significantly reduced with ARCs as compared to that on the bare solar cell surface. Also, multilayer ARCs with "step-down" structures ($n_{ambient} < n_m < n_{m-1}$ < … < $n_2 < n_1 < n_s$) achieve more broadband low reflectance than the single-layer ARC. Therefore, they are widely used for multi-junction solar cells where broadband low reflectance is required.
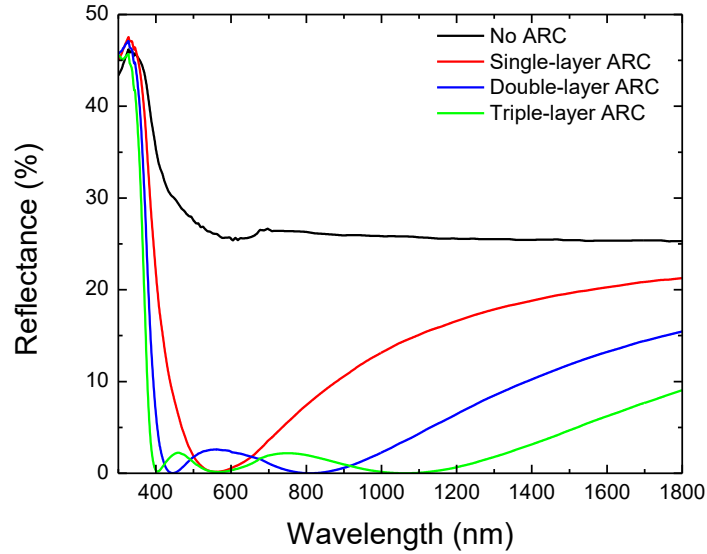
Figure 1.1 – Calculated reflectance of antireflection coatings with different number of layers optimized for a target wavelength of 550 nm.

1.1.2 Introduction to III-V Multi-junction Solar Cell

Over the past decades, the world's ever-increasing energy demands and the abundance of sunlight have driven enormous developments in solar cell technology. III-V multi-junction solar cells, holding the world record efficiency 46 % [7], have been one of the most important and innovated solar cells in both space [8-11] and terrestrial concentrated photovoltaic applications [10,12,13]. Multi-junction solar cells are composed of multiple sub-cells that are connected in series. Each sub-cell is a p-n junction. As light penetrates into a sub-cell, photons with energy larger than the material's bandgap will be absorbed and generate electron-hole pairs that provide electrical current as separated towards two electrodes. The excess photon energy larger than the bandgap will be lost to lattice vibration and dissipated as heat. On the other hand, photons with energy lower than the bandgap will not be absorbed and the energy gets lost.

3

Multi-junction solar cells have multiple sub-cells with decreasing bandgaps from top to bottom, absorbing light with decreasing photon energies. Therefore, they are enabled to take advantage of a wider spectral range of sunlight than single-junction solar cells.

Nowadays, the state-of-art III-V triple-junction solar cells achieve over 30 % and 41.6 % with AM0 space and AM1.5 terrestrial solar spectra, respectively [10,12]. The sub-cells have bandgaps of 1.9 eV/1.4 eV/0.7 eV. Further efficiency improvements would be realized through adding more junctions with optimized bandgaps. A 1.9 eV/1.4 eV/1.1 eV/0.7 eV 4-junction (4J) wafer-bonded solar cell has achieved the world record efficiency 46 % at 508 suns under AM1.5 spectrum [7]. Also, under AM0 space spectrum, a record efficiency of 36 % has been achieved by a 2.2 eV/1.7 eV/1.4 eV/1.0 eV/0.7 eV 5-junction (5J) wafer-bonded solar cell [11].

Multi-junction solar cells present more challenges for ARCs than single-junction solar cells. First, the wider spectral range of light conversion requires more broadband ARCs, which necessitates multilayer ARCs rather than single-layer ARCs. Second, the series-connected sub-cells demand current matching. Solar cell efficiency is proportional to the short-circuit photocurrent density J_{SC}. For a multi-junction solar cell, J_{SC} is the minimal of all sub-cells. For one sub-cell, it can be calculated as [14]

$$J_{SC} = q \int \frac{I(\lambda)}{E_{ph}(\lambda)} \cdot T(\lambda) \cdot IQE(\lambda) \cdot d\lambda$$

Eq. 1.5

where I is the irradiance, E_{ph} is the photon energy, IQE is the internal quantum efficiency, λ is the wavelength, and q is the electronic charge. T = 1 – R – A – S is the optical transmittance of ARC, in which R is the optical reflectance, A is the optical absorption, respectively, and S is the internal scattering due to density fluctuations (e.g. pores) in the

ARC. In order to maximize J_{SC}, ARCs are designed to preferentially maximize the optical transmittance within the spectral range of the current limiting sub-cell.

In this study, the multilayer ARC is designed for an inverted metamorphic 4J space solar cell (IMM4JSC) [9]. The cross-sectional schematic graph and IQE of the IMM4JSC are shown in Figure 1.2(a) and Figure 1.2(b) along with the AM0 space solar spectrum. The AlInP (30 nm) / GaInP substrate is used as the simplified structure of IMM4JSC for ARC designing. With 100% transmittance of sunlight, J_{sc} of the sub-cells from top to bottom are 16.9 mA/cm^2, 15.7 mA/cm^2, 18.0 mA/cm^2, 20.3 mA/cm^2, respectively, indicating 1.5-eV AlGaAs sub-cell 2 to be the current-limiting sub-cell. Therefore, optical transmittance within the spectrum range of the 1.5-eV AlGaAs sub-cell 2 needs to be maximized.
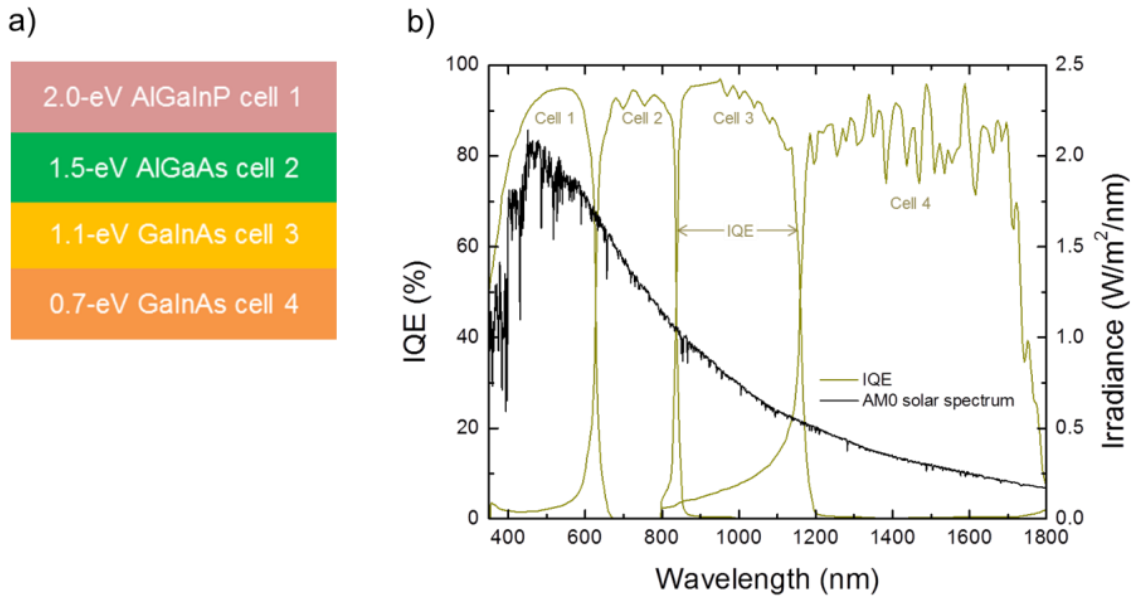
Figure 1.2 – (a) Cross-section schematic of an inverted metamorphic 4-junction space solar cell; (b) IQE of an inverted metamorphic 4-junction space solar cell and AM0 solar spectrum.

1.2 Designing of Multilayer Al$_2$O$_3$/TiO$_2$/Al$_2$O$_3$ Antireflection Coating with Herpin Equivalent Layers

ARCs are designed to maximize J$_{SC}$ of solar cells. A general figure of merit in ARC designing is solar-weighted reflectance (SWR) (adapted from [14]), which can be calculated as

$$SWR = 1 - \frac{J_{SC}}{J_{SC,T=100\%}}$$

where J$_{SC, T=100\%}$ is short-circuit photocurrent density with 100 % optical transmittance. With refractive indices optimized using the relationship of $n_j^2 = n_{j-1}n_{j+1}$, optimal thicknesses of ARCs can be determined that minimize SWR. Figure 1.3 shows the optimized ARCs with different number of layers for IMM4JSC along with the SWR values. n values correspond to the wavelength of 550 nm. The double-layer ARC increases SWR by an absolute of 2 % with respect to the single-layer ARC while the triple-layer ARC further increases SWR by only 0.1 %. The absolute change in SWR is approximately equal to that in solar cell efficiency. With less complexity and time of fabrication, double-layer ARCs are widely used for multi-junction solar cells.

Single-layer ARC	Double-layer ARC	Triple-layer ARC

$n_3 = 1.35$ 72 nm

$n_2 = 1.49$ 82 nm $n_2 = 1.83$ 51 nm

$n_1 = 1.83$ 85 nm $n_1 = 2.24$ 54 nm $n_1 = 2.48$ 36 nm

$n_{sub} = 3.36$ $n_{sub} = 3.36$ $n_{sub} = 3.36$

SWR = 2.4 %   *SWR = 0.4 %*   *SWR = 0.3 %*
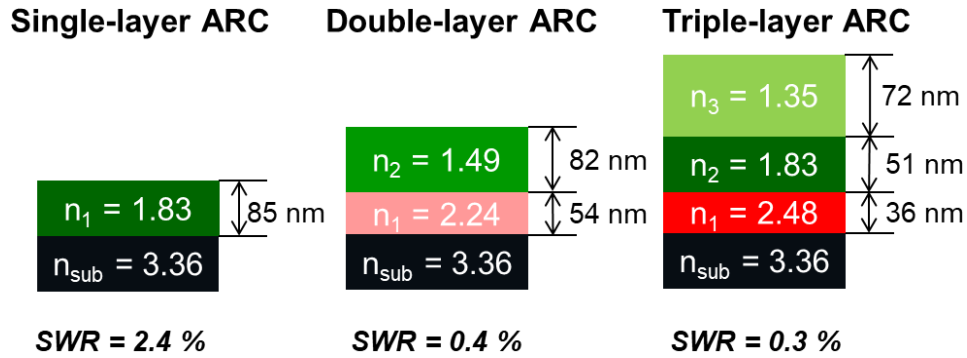
Figure 1.3 – Optimized layers and SWR of single-layer, double-layer and triple-layer antireflection coatings for an inverted metamorphic 4-junction space solar cell. The n values correspond to the wavelength of 550 nm.

Among various types of ARCs [5,14-17], homogeneous thin films with suitable optical properties are commonly used for III-V multi-junction solar cells. As shown in Figure 1.4, TiO_2 and Al_2O_3 deposited by atomic layer deposition (ALD) [18] have nearly suitable refractive indices for the high-index and low-index materials, respectively. Also, TiO_2 and Al_2O_3 films with these refractive indices are typically associated with non-porous and stoichiometric films [19]. The absence of pores enables to avoid internal scattering while the stoichiometry ensures proper bandgaps (~ 3.2 eV for TiO_2 and ~ 7 eV for Al_2O_3) to achieve non-absorption throughout Vis/IR for TiO_2 and UV/Vis/IR for Al_2O_3. These properties, along with the feasibility of ALD to deposit non-porous and stoichiometric films, the compatibility with present solar cell production methods, and the chemical and mechanical stability in the solar cell environment [20], make TiO_2 and Al_2O_3 good candidates for the multilayer ARCs of space multi-junction solar cells.
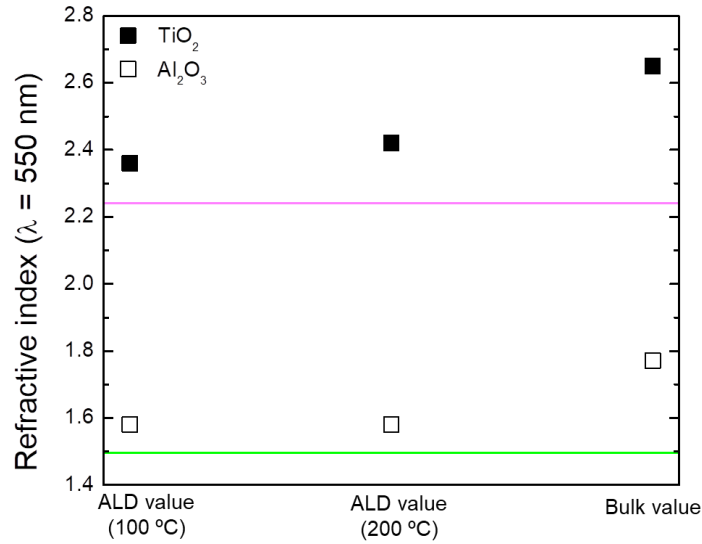
Figure 1.4 – Optimum refractive indices (λ = 550 nm) of the high-index material (the pink line) and the low-index material (the green line) of the "step down" double-layer antireflection coating for an inverted metamorphic 4-junction space solar cell, and the refractive indices of TiO_2 (solid squares) and Al_2O_3 (open squares) of atomic layer deposited films and bulk crystals.

Furthermore, simulation indicates that SWR can be improved by an absolute of 1 – 2 % with optimum index values achieved. Since the optimum high index value is in between TiO_2 and Al_2O_3, it can be matched with Herpin equivalent layers. Epstein [21] showed that mathematically a symmetrical combination of non-absorbing thin films can be equal to one non-absorbing layer, where the equivalent structures are referred to as Herpin equivalents. In optical film designing, Herpin equivalents are commonly used in achieving an intermediate refractive index with no materials available through a symmetric combination of high index and low index materials [20,22]. The schematic graph in Figure 1.5 (a) shows the application of Herpin equivalent layers to the "step-

8

down" double-layer ARC. The n values correspond to the wavelength of 550 nm. A symmetric $Al_2O_3/TiO_2/Al_2O_3$ is designed to achieve the optimum high index value. Together with top Al_2O_3 as the low index layer, the result is an asymmetric $Al_2O_3/TiO_2/Al_2O_3$. The "step-down" double-layer ARC and the mathematically equivalent asymmetric $Al_2O_3/TiO_2/Al_2O_3$ are physically equivalent with nearly the same optical reflectance as shown in Figure 1.5 (b) and also an identical SWR of 1.0 %. Considering the high cost of III-V multi-junction solar cells and the feasibility of depositing Al_2O_3 and TiO_2 by ALD, Herpin equivalent is worth applying to the multilayer ARC. Optical properties of the asymmetric $Al_2O_3/TiO_2/Al_2O_3$ antireflection stack designed for IMM4JSC would be characterized in this study.
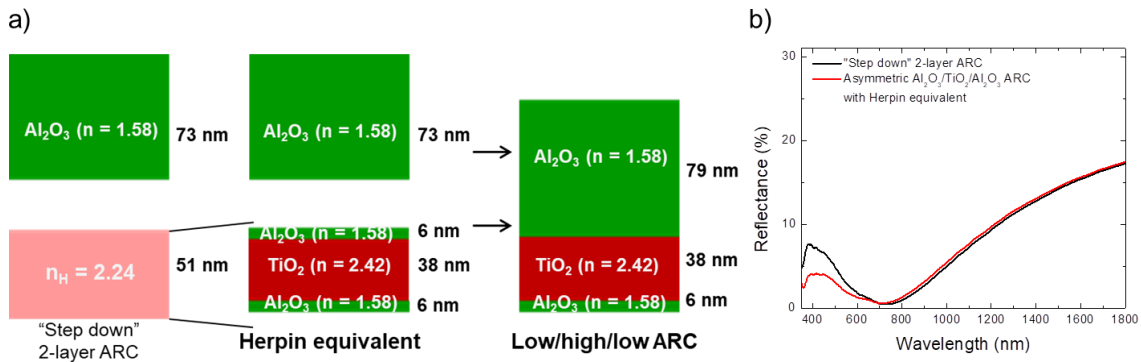
Figure 1.5 – a) Schematic graphs illustrating the asymmetric $Al_2O_3/TiO_2/Al_2O_3$ antireflection coating as derived from a "step down" double-layer structure using the Herpin equivalent concept. The n values correspond to the wavelength of 550 nm. b) Calculated reflectance of the "step down" 2-layer antireflection coating and the mathematically equivalent asymmetric $Al_2O_3/TiO_2/Al_2O_3$ ARC with Herpin equivalent. The SWR of both ARCs is 1.0 %.

1.3 Atomic Layer Deposition

ALD is a chemical vapor deposition (CVD) technique realized with self-controlled surface reactions. First invented in 1980s for the depositions of both polycrystalline ZnS and amorphous dielectric films in electroluminescent flat panel displays [23], it has been widely used in various applications such as battery electrodes [24,25], photocatalysts [26,27], transistors [28,29], and optical coatings [18,30]. Several types of materials can be deposited by ALD including metals [31,32], metal oxides [18,24-26,28-30], metal nitrides [25,33], metal sulfides [34], and metal phosphates [35,36]. The main advantages of ALD over other deposition techniques (e.g. plasma enhanced CVD, spin coating) are the sub-nanometer thickness control, the ability to deposit non-porous and stoichiometric films, large-area uniformity, and low deposition temperatures (typically below 400 ℃). Benefiting from these advantages, ALD is quite suitable for depositing ARCs used for space multi-junction solar cells.

An ALD process consists of individual saturated surface reactions between the substrate and different precursors. These reactions perform sequentially. Figure 1.6 schematically shows the thermal ALD process of Al_2O_3 deposited on Si with water and trimethylaluminum (TMA) as precursors. This process involves: (1) The sample surface is hydroxylated from exposure to air, oxygen or ozone (Figure 1.6 (a)); (2) The TMA precursor is pulsed in and reacts with the OH groups on the surface (Figure 1.6 (b) and Figure 1.6 (c)). Since it does not react with itself, the monolayer product passivates the surface; (3) Unreacted TMA molecules are removed by evacuation and/or purging with nitrogen (Figure 1.6 (d)); (4) Water is pulsed in. The Al-O-Al bridges form and the surface is passivated with Al-OH. Also, CH_3 is removed through a gaseous byproduct

CH_4 (methane) (Figure 1.6 (e) and Figure 1.6 (f)); (5) Unreacted H_2O and CH_4 molecules are removed through evacuation and/or purging with nitrogen (Figure 1.6 (g)). These five steps form a cycle and will be repeated throughout the ALD process. Due to the nature of saturated reactions, ALD can be considered as a layer by layer growth technique. The layer thickness increases linearly with the number of cycles.
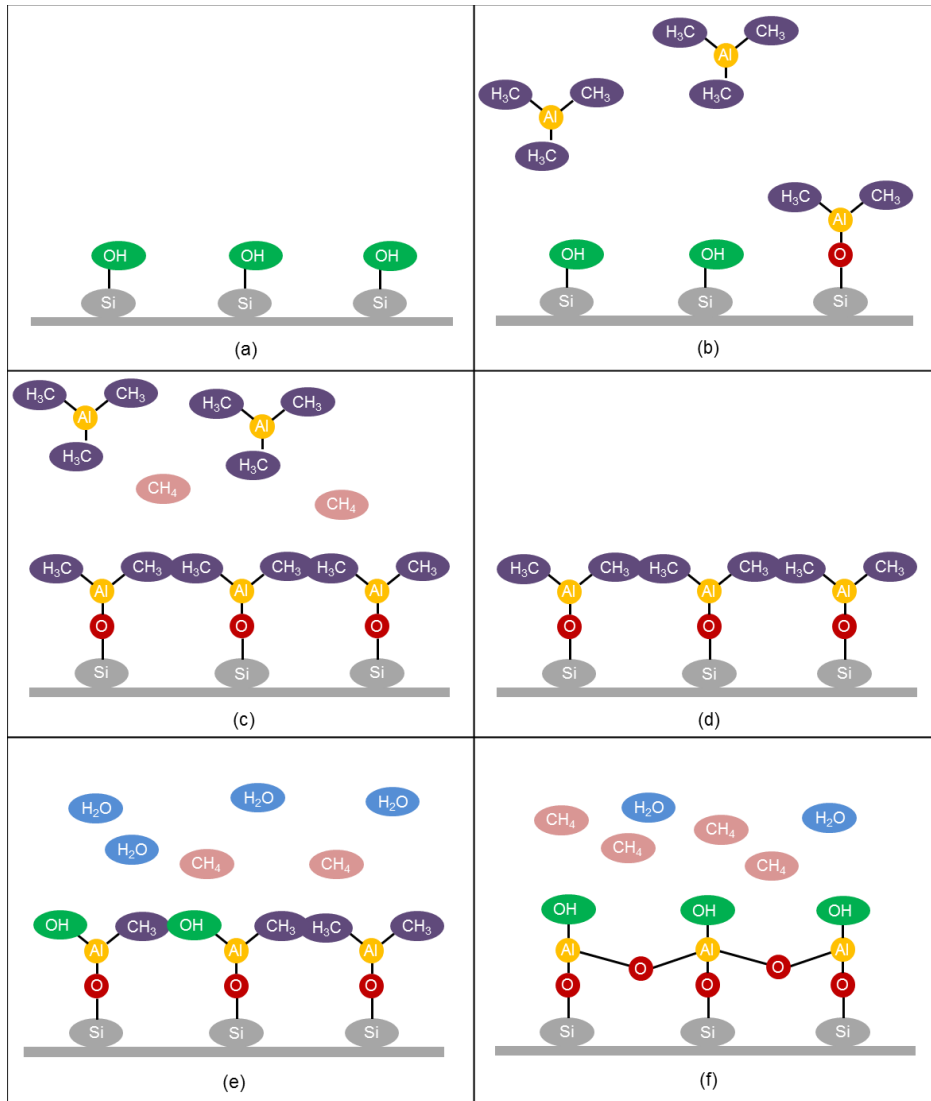
Figure 1.6 – Schematic of thermal ALD process of Al_2O_3 with trimethylaluminum and H_2O as precursors.

In practice, optical properties of ALD layers are affected by deposition parameters (e.g. temperature, type of precursors, and the time length of cycles) that determine the nature and extent of chemical reactions each cycle. It has been reported that deposition temperatures below approximately 200 ºC would induce hydroxyl group and higher [O]/[Al] ratio than stoichiometry in the Al_2O_3 layer, which is probably due to the incomplete reaction between TMA and the Al-OH surface groups with slow reaction kinetics at low temperatures [37-39]. The incorporation of hydroxyl groups and higher [O]/[Al] ratio than stoichiometry results in lower mass densities [37-39], refractive indices [37,38], and bandgaps [40]. Besides, layer thicknesses are also influenced by the deposition parameters that affect the growth per cycle (GPC). It has been reported that a maximum GPC of Al_2O_3 with thermal ALD is achieved at a specific temperature, which is explained by the slower reaction kinetics at lower temperatures and the lower surface coverage of Al-OH and Al-CH$_3$ at higher temperatures [37-39].

1.4   Optimization of Optical Properties

Layer thicknesses and refractive indices usually deviate from anticipated values due to fabrication issues, which influences the optical performance of multilayer ARCs. Figure 1.7 shows that with the refractive indices varying from ALD [18] to bulk values (displayed in Figure 1.2), the reflectance minima of an Al_2O_3 (70.0 nm)/TiO_2 (43.8 nm)/Al_2O_3 (6.8 nm) antireflection stack on IMM4JSC shifts from 700 nm to 400 nm together with an absolute increase of over 3 % in SWR. Therefore, it is important to optimize the optical properties of ARCs in order to minimize SWR and improve solar cell efficiencies by as much as over 3 %.
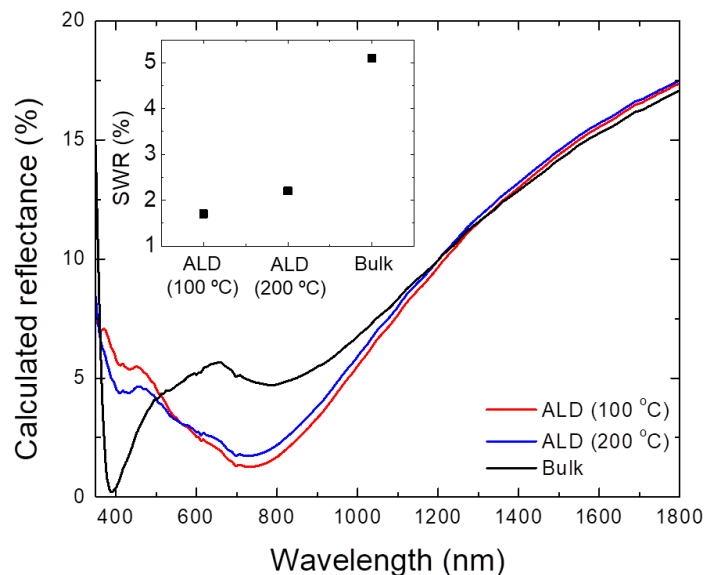
Figure 1.7 – Calculated reflectance and SWR of an Al_2O_3(70.0 nm)/TiO_2(43.8 nm)/Al_2O_3(6.8 nm) antireflection stack on an inverted metamorphic 4-junction space solar cell with refractive indices of ALD films deposited at different temperatures and the bulk crystals.

Two approaches are commonly used for optimizing optical properties: (1) modifying ALD parameters; (2) post-annealing. As discussed in Section 1.3, ALD parameters influence layer densities, refractive indices, bandgaps, and GPCs. Modifying those parameters would be an effective approach in optimizing optical properties to the designed values. On the other hand, post-annealing has been reported to densify thin films through crystallization [41,42] and removal of voids [43,44] and hydroxyl groups [45,46].

1.5   X-Ray Scattering Techniques

Layer thicknesses and refractive indices need to be accurately characterized in optimizing optical properties of ARCs. This can be realized by several conventional

techniques such as spectroscopic ellipsometry (SE) and spectrophotometry [47,48]. In addition, layer densities are typically correlated with refractive indices. They are also important to be accurately determined.

X-ray reflectivity (XRR) is a powerful technique that non-destructively measures film densities with less than a few percent uncertainty. It also determines layer thicknesses and surface and interface roughnesses and/or grading with sub-nanometer precision. As diffraction is not involved, XRR works well for ARCs that are typically amorphous. In practice, simulation programs are utilized to obtain the information from the specular XRR pattern, which shows interference fringes that stem from reflections from multiple layers with different densities. While this works well for some applications, problems modeling the structure arise when lacking in information of the number of layers and layer thicknesses. Other layers forming at surface or interfaces also contribute to the overall specular XRR pattern. Fortunately, recent developments have shown that with proper processing of the data, a Fourier transform (FT) approach developed by Poust et al. [49] can provide straightforward information about the layer thicknesses, which greatly assists in XRR modeling. Its effectiveness has been demonstrated for III-V multi-layers in metamorphic high-electron-mobility transistors [49]. Combining the FT approach with specular XRR simulation would be a powerful approach in layer thickness determination of multilayer systems. Together with the ability to determine density and surface and interface roughness and/or grading, this XRR approach works well for ARCs with densities from 65 % to over 90 % of bulk values [18,38,50]. More details of XRR will be addressed in Chapter 2.

Besides optical reflectance, internal scattering induced by density modulations (e.g. pores) in ARCs would also affect the optical transmittance of broadband ARCs. It is detrimental to the optical performance of ARCs particularly in the lower spectral range (UV/Vis) of space multi-junction solar cells which is usually absorbed by the current limiting sub-cells. ARCs have lower densities than bulk values [18,38,50], for which they are suggested to be porous, non-stoichiometric, and/or incorporated with hydrogen-containing species. While internal scattering would not be induced by non-stoichiometry and hydrogen-containing species in homogenous films, pores with sizes larger than approximately 1/10 of the wavelength would cause internal scattering. Therefore, the pore sizes in the layers that make up the ARCs need to be quantified. Grazing-incidence small angle X-ray scattering (GISAXS) is able to non-destructively characterize the pore size distribution in the range from sub-nanometer to hundreds of nanometers [51]. It works well for thin films with the capability of measuring closed pores that cannot be assessed by conventional Brunauer–Emmett–Teller (BET) techniques, and pores with small sizes (less than approximately 10 nm), low porosity (on the order of several % or less) and unknown spatial distributions that scanning electron microscopy (SEM) and transmission electron microscopy (TEM) can hardly observe. Previously GISAXS was applied to low-k dielectric films, in which pore scattering was measured by X-ray diffuse scans [52-54]. However, a challenge associated with the prior GISAXS methods exists in separating diffuse scattering from surface and interface roughnesses as both can also contribute to the measured total diffuse scattering in addition to pore scattering. A more detailed introduction to GISAXS will be presented in Chapter 3. Also, a combined

method of GISAXS, atomic force microscopy (AFM), and XRR developed in this study will be introduced.

1.6 Motivation

Optimization of the $Al_2O_3/TiO_2/Al_2O_3$ multilayer ARC could improve the efficiency of IMM4JSC by over 3 % as discussed in Section 1.4. It is therefore important to determine how optical properties of ARCs are influenced by the optimization methods, for which layer properties need to be accurately characterized. The XRR method combining the FT approach developed by Poust et al. [49] and specular XRR simulation provides an effective approach in obtaining layer thicknesses, densities, and surface and interface roughnesses and/or grading of multilayers. It gives a good insight into the layer properties making up the ARCs together with other conventional techniques including SE and spectrophotometry. In addition, the easier modeling in XRR simulation would greatly facilitate the determination of layer properties benefiting from the FT approach. In this study, the XRR method was applied to the multilayer ARCs.

Pore size distribution in ARCs is important in assessing internal scattering that would undermine optical transmittance. However, it has been rarely studied for the ALD ARCs even though pores could exist as suggested by the lower densities than bulk values. GISAXS serves as a powerful tool in characterizing pore size distribution in thin films which is quite applicable to ARCs. Nevertheless, modifications are needed for the GISAXS approaches addressing the challenge of separating the diffuse scattering from surface and interface roughnesses from pore scattering in prior studies.

Finally, it is necessary to fully characterize optical properties of ARCs by other techniques that can also validate the X-ray scattering techniques. In this study, SE,

spectrophotometry, glancing incidence X-ray diffraction (GIXRD), TEM with bright field TEM (BFTEM) images, selected area electron diffraction (SAED), high-resolution TEM (HRTEM) images, and scanning TEM-energy dispersive X-ray spectroscopy (STEM-EDX) were also applied to ARCs.

1.7   Dissertation Outline

In this thesis, introduction to the X-ray scattering methods and characterization of multilayer Al_2O_3/TiO_2/Al_2O_3 ARCs deposited by ALD are provided. Chapter 2 presents the principle of specular XRR and the FT approach. In Chapter 3, the principle of GISAXS is introduced, and a new method combining GISAXS with AFM and XRR is developed addressing the challenge in prior approaches. Chapter 4 describes experimental details, including the sample fabrication and the measurement apparatus. Chapter 5 discusses properties of individual Al_2O_3 and TiO_2 layers deposited on Si substrates and influences of the optimization methods on layer properties. Chapter 6 and Chapter 7 address optical properties of multilayer Al_2O_3/TiO_2/Al_2O_3 ARC deposited on Si substrate and III-V substrates, respectively. Also, influences of optimization methods on the multilayer ARC are assessed. Finally, the conclusion and the future work are provided in Chapter 8.

Chapter 2 X-Ray Reflectivity

2.1 Introduction to X-Ray Reflectivity

X-ray refers to the electromagnetic wave within the wavelength range from 0.01 – 10 nm (10^{16} – 10^{19} Hz). It would be reflected as incident onto the surface of a different medium, which is similar to the light in UV/Vis/IR range. Due to the high frequency, the refractive index of X-ray originates from the response of electrons in materials to the electromagnetic wave, which can be written as

$$N = 1 - \delta - i\beta \qquad \text{Eq. 2.1}$$

with

$$\delta = \frac{r_e \lambda^2}{2\pi} N_A \sum_i \frac{\rho_i}{A_i} (Z_i + f_i^{'}) = \frac{r_e \lambda^2}{2\pi} \rho_e \qquad \text{Eq. 2.2}$$

$$\beta = \frac{r_e \lambda^2}{2\pi} N_A \sum_i \frac{\rho_i}{A_i} f_i^{''} = \frac{\lambda}{4\pi} \mu \qquad \text{Eq. 2.3}$$

where ρ_e is the electron density, r_e is the classical radius of electron (2.8×10^{-15} m), λ is the wavelength of the electromagnetic wave, and μ is the mass absorption coefficient. δ is generally on the order of 10^{-5} and β is approximately one order of magnitude smaller than δ. The refractive index of X-ray is therefore slightly less than 1 as compared to that in UV/Vis/IR (10^{11} – 10^{16} Hz) range larger than 1. Thus, total reflection occurs for X-ray as the incident angle ω between the incident beam and the surface of a medium below a critical angle ω_c. According to Snell-Descartes' law

$$n_1 \cos \omega = n_2 \cos \omega^{'} \qquad \text{Eq. 2.4}$$

where $\omega^{'}$ is the refracted angle between the refracted beam and the surface of the medium. Since $n_1 = 1$ in air and $n_2 = 1 - \delta$ (absorption not considered) in the medium

$$\cos \omega_c = n = 1 - \delta$$

<div align="right">Eq. 2.5</div>

At small angles,

$$\cos \omega_c \approx 1 - \omega_c^2 / 2$$

<div align="right">Eq. 2.6</div>

Therefore,

$$\omega_c = \sqrt{2\delta} = \lambda \sqrt{\frac{r_e \rho_e}{\pi}}$$

<div align="right">Eq. 2.7</div>

Above the critical angle, reflectivity drops rapidly below one. Eq. 2.7 indicates that (electron) density of a medium can be determined from the critical angle.

XRR measures specular intensity with symmetric θ:2θ scans, in which the scattered angle 2θ between the incident beam and the scattered beam keeps twice as much as the incident angle ω. Based on Maxwell equations and interfacial continuity conditions, Parratt [55] solved the reflected to incident amplitude ratio at the top of layer j, X_j, for specular XRR,

$$X_j = \frac{r_j + X_{j-1} \exp(2ik_{z,j}t_j)}{1 + r_j X_{j-1} \exp(2ik_{z,j}t_j)}$$

<div align="right">Eq. 2.8</div>

The component of the wave vector perpendicular to the surface in layer j, $k_{z,j}$, is

$$k_{z,j} = \frac{2\pi}{\lambda \sqrt{n_j^2 - \cos^2 \omega}}$$

<div align="right">Eq. 2.9</div>

where n_j is the refractive index of layer j at wavelength λ. The Fresnel reflection coefficient from the sharp interface between layers j + 1 and j, r_j can be calculated as

$$r_j = \frac{k_{z,j+1} - k_{z,j}}{k_{z,j+1} + k_{z,j}}$$

<div align="right">Eq. 2.10</div>

For rough and/or graded surface and interfaces, it can be modified [56] as

<div align="center">19</div>

$$r_j = \frac{k_{z,j+1} - k_{z,j}}{k_{z,j+1} + k_{z,j}} \exp\left[-2\sigma_j \sqrt{k_{z,j+1} k_{z,j}}\right]$$
<div align="right">Eq. 2.11</div>

where σ_j is the surface or interface roughnesses and/or grading. For a multilayer system with m layers, the reflectivity R is equal to $|X_m|^2$ in which X_m is the amplitude ratio at the surface. This is also referred to as dynamic theory as multiple reflections at surface and interfaces are considered. Based on the dynamic theory, specular XRR can be simulated. In this study, a Jordan Valley REFS 4.5 software was used to perform the XRR simulation.

Figure 2.1 shows the simulated specular XRR of a 74.0-nm-thick Al_2O_3 layer on a Si substrate with respect to the vertical reciprocal space coordinate Q_z ($Q_z = 4\pi\sin\omega/\lambda$). The Al_2O_3 film has a density of 2.94 g/cm^3 as compared to 2.33 g/cm^3 of Si. Interference fringes in the reflectivity curve are formed by the scattered beams from the Al_2O_3 layer and the Si substrate with different densities. The XRR pattern is affected by the layer thickness, the density contrast with adjacent media, and surface and interface roughnesses and/or grading. Effects of these properties on the reflectivity curve are presented in Figure 2.1. For a multilayer system, the reflectivity is determined by the interference of scattered beams from multiple layers and the substrate. Layer thicknesses, densities and surface and interface roughnesses and/or grading are generally determined through least squares fitting of the experimental specular XRR that minimizes the mean-absolute error of the log-transformed data (MAE_{log}) [57] which can be expressed as

$$MAE_{log} = \frac{1}{N-1} \sum_{j=1}^{N} \left| \log I(\text{experiment})_j - \log I(\text{simulation})_j \right|$$
<div align="right">Eq. 2.12</div>

where N is the total number of data points, and I(experiment)$_j$ and I(simulation)$_j$ are the jth data points of experimental and simulation data, respectively. Specular XRR is

applicable to any thin films with roughnesses and/or grading smaller than ~ 5 nm and density contrast larger than ~ 10 % between adjacent layers. Particularly, the ability of layer density determination is unique to this technique.
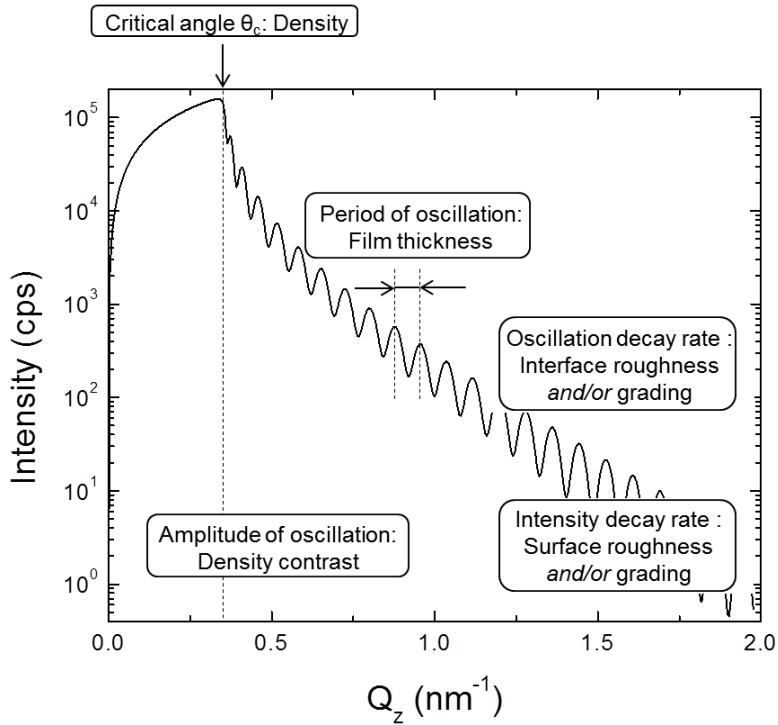
Figure 2.1 – Simulated specular XRR of a 74.0-nm-thick Al_2O_3 layer on a Si substrate. The density of Al_2O_3 layer is 2.94 g/cm^3. The influences of layer properties on the reflectivity curve are also presented.

While specular XRR simulation works well for some applications, problems arise in modeling the structure when lacking in information of the number of layers and layer thicknesses. Other surface and interfacial layers would also contribute to the overall XRR patterns. In many cases, it is not straightforward to obtain a model that achieves an acceptable fit.

2.2 An Enhanced Algorithm for Layer Thickness Determination

2.2.1 Discrete Fourier Transform

The oscillation frequencies in XRR with respect to Q_z are equal to the spacing between surface and interfaces of the thin films. FT power spectra of the specular XRR would thus yield peaks representing both thicknesses of individual layers and thickness sums of multiple layers. This provides information about the number of layers and layer thicknesses. For example, a single layer would yield one peak in the FT power spectrum that represents the layer thickness. A double-layer system, on the other hand, would yield three peaks representing thicknesses of two individual layers and their thickness sum. Benefiting from the thickness information from FT, it is much easier for XRR modeling.

Practically, discrete FT (DFT) is applied to the discrete data points of experimental XRR [49]. It is calculated as

$$DFT(t) = \left[\frac{1}{N} \sum_{Q_{z,1}}^{Q_{z,N}} I(Q_z) \cos(tQ_z) \right]^2 + \left[\frac{1}{N} \sum_{Q_{z,1}}^{Q_{z,N}} I(Q_z) \sin(tQ_z) \right]^2 \qquad \text{Eq. 2.13}$$

where N is the number of data points. Considering refraction, Durand [58] converted the grazing incidence incident angle ω to Q_z with

$$Q_z = \frac{4\pi \sqrt{\cos^2 \omega_c - \cos^2 \omega}}{\lambda} \qquad \text{Eq. 2.14}$$

where the critical angle ω_c is chosen as the angular value with half of the total reflected intensity. Figure 2.2 shows DFT power spectrum of the simulated reflectivity curve in Figure 2.1. Unfortunately, the thickness peak at t = 74.0 nm is buried by a strong artifact of "zero thickness" peak which is attributed to the truncation rod [59] corresponding to

the sloping background in specular XRR. Therefore, the effect of truncation rod needs to be removed before applying DFT.
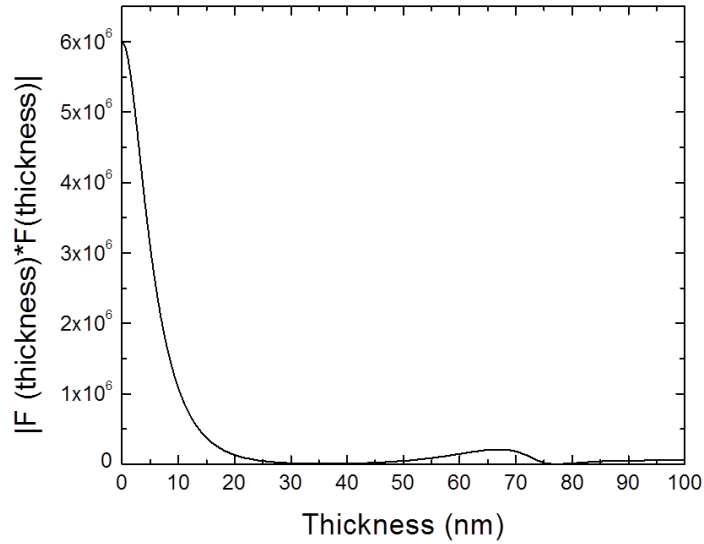
Figure 2.2 – DFT power spectrum of the simulated specular XRR of a 74.0-nm-thick Al$_2$O$_3$ layer on a Si substrate.

2.2.2 An Enhanced Discrete Fourier Transform Approach

Several approaches have been reported to enhance the DFT algorithm by removing the truncation rod in specular XRR. Banerjee et al. [60] proposed subtraction of the off-specular longitudinal scan. The off-specular longitudinal scan moves 2θ twice as fast as ω with ω offset from half of 2θ. The scattering intensity measured by the off-specular longitudinal scan has a similar shape as the truncation rod and does not show interference fringes for the thin films that have no vertically correlated surface and interface roughnesses [49]. Therefore, the effect of truncation rod can be reduced by subtracting the off-specular scan from the specular scan. However, this method loses its effectiveness as the thin films have vertically correlated surface and interface

roughnesses [49]. Another method proposed by Grave de Peralta et al. [61] was a combination of logarithmic compression and average subtraction. As shown in Figure 2.3, the intensity of the truncation rod in Figure 2.1 is well estimated with logarithmic compression followed by averaging equal number of adjacent data points on both sides of one data point. A very distinguishable thickness peak appears in the DFT power spectrum and no artifact of "zero thickness" peak shows up. This method works well for many cases, but not for very thin layers with periods of oscillations approaching the scan length, and superlattice structures that have superlattice peaks elevating the average curve above the background slope [49].
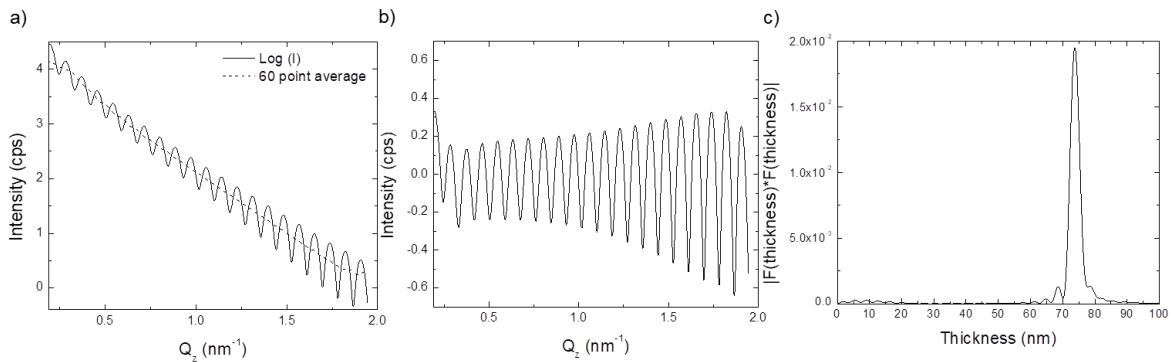
Figure 2.3 – (a) Logarithmically compressed simulated specular XRR of a 74.0-nm-thick Al_2O_3 layer on a Si substrate with 60 point local average; (b) The intensity of logarithmically compressed specular XRR subtracted by 60 point local average; (c) DFT power spectrum of the curve in (b).

Durand et al. [58] introduced the method of multiplication of Q_z^4. The main advantage of this method is the independence of oscillation period lengths [49]. Nevertheless, as shown in Figure 2.4, DFT power spectrum of the reflectivity curve in

Figure 2.1 multiplied by Q_z^4 still yields a strong artifact of "zero thickness" peak, as compared to the weak thickness peak from the layer.

a)

b)
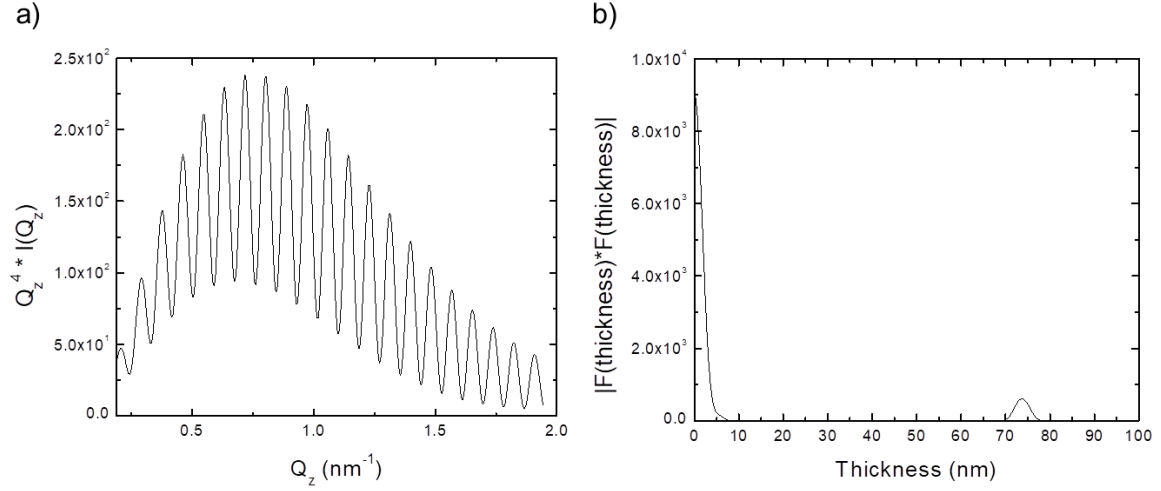
Figure 2.4 – (a) Simulated specular XRR of a 74.0-nm-thick Al_2O_3 layer on a Si substrate multiplied by Q_z^4; (b) DFT power spectrum of the curve in (a).

A recent development demonstrated by Poust et al. [49] has shown that the truncation rod can be effectively removed combining multiplication of Q_z^4 and differentiation with respect to Q_z. Following the multiplication of Q_z^4, the XRR data is differentiated with each data point transformed by

$$I_p^T = \frac{dI_p}{dQ_{Z,p}} = \frac{1}{N}\sum_{i=1}^{N}\frac{I(Q_{Z,p+i})-I(Q_{Z,p-i})}{Q_{Z,p+i}-Q_{Z,p-i}}$$

Eq. 2.15

The summation on the right side of Eq. 2.15 is over N nearest data points on either side of the pth data point. The number of data points used to calculate the average slope at the pth data point should be high enough to average out noise fluctuations, but kept below the period lengths of any possible thickness signals. As shown in Figure 2.5, this method is extremely effective in reducing the effect of truncation rod in Figure 2.1 as well as

amplifying layer thickness fringes. A very distinguishable and sharp peak is present at the correct thickness. Also, no artifact of "zero thickness" peak shows up in the DFT power spectrum.
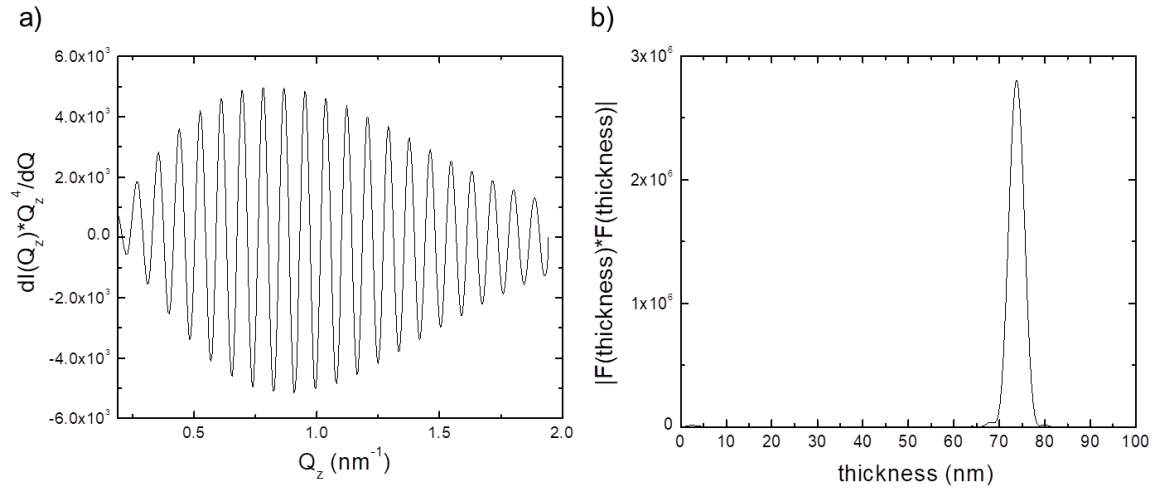
Figure 2.5 – (a) Differentiation of simulated specular XRR of a 74.0-nm-thick Al_2O_3 layer on a Si substrate multiplied by Q_z^4; (b) DFT power spectrum of the curve in (a).

Chapter 3 Grazing-Incidence Small Angle X-Ray Scattering

3.1 Introduction to Grazing-Incidence Small Angle X-Ray Scattering

Small angle X-ray scattering (SAXS) is able to characterize the size distribution of density fluctuations in materials from sub-nanometer to hundreds of nanometers [51]. It has been widely used for different kinds of materials from liquids [62,63] to solids [52,64]. Conventionally, a transmission geometry was used in SAXS measurements [64] while it is not suitable for thin films due to the absorption of substrates [52,65]. SAXS works well for thin films when combined with the surface sensitivity of grazing-incidence diffraction under reflection geometry [66]. In 1989, Levine et al. [67] first reported the GISAXS study on the growth of gold islands on glass.

The determination of size distribution of density fluctuations requires a suitable theory for the X-ray scattering process. Under reflection geometry, reflection and refraction at film surface and interfaces need to be considered. Theoretically X-ray scattering intensity can be calculated with distorted wave Born approximation (DWBA) [52,65]. The scattering is proportional to the square of structure factor F which is dependent on shapes and sizes of scattering features. Specifically for scattering features with a spherical shape, the structure factor F (Q) as a function of reciprocal space coordinate Q (Q = 4πsinθ/λ, θ is half of the scattered angle 2θ) can be expressed as

$$F(Q) = \frac{4\pi D^3}{(QD)^3}\left[\sin(\frac{QD}{2}) - \frac{QD}{2}\cos(\frac{QD}{2})\right] \qquad \text{Eq. 3.1}$$

where D is the diameter of scattering features. If a size distribution is introduced, the structure factor F (Q) can be replaced by

$$\overline{F}(Q) = \int_0^\infty F(Q,D)M(D,D_0,\sigma_0)\,dD \qquad \text{Eq. 3.2}$$

where M is the size distribution with an average diameter of D_0 and a standard deviation of σ_0. Through fitting the measured scattering with a least squares minimization method, the size distribution of scattering features can be obtained.

Conventionally GISAXS measures 2-dimensional (2D) scattering intensity with the synchrotron source [68-70], in which the incident angle is fixed near the critical angle ω_c and the scattered intensity is recorded by a 2D detector. Size distribution along both out-of-plane and in-plane directions can be obtained. On the other hand, X-ray diffractometers with a 1-dimensional (1D) configuration and laboratory sealed tube source have also been used for GISAXS studies [52,54] benefiting from the developments in X-ray generators and optics. Scan modes used in 1D GISAXS studies include longitudinal (offset $\theta:2\theta$) scan which is introduced in Section 2.2.2, radial (2θ) scan, and transverse (ω) scan. Radial scan moves 2θ with ω fixed, and transverse scan moves ω with 2θ fixed. Figure 3.1 (a) represents longitudinal scan, radial scan, transverse scan, and specular scan in reciprocal space. The specular scan measures specular intensity along the Q_z axis while the longitudinal scan, the radial scan, and the transverse scan measure diffuse scattering intensities along different directions other than the specular intensity. This can be determined using Ewald sphere construction [71]. As shown in Figure 3.2 (b), the incident beam vector k_o with a magnitude of $1/\lambda$ is set to the origin O in reciprocal space, and the scattered beam vector k_h with the same magnitude is connected to the incident beam vector. The angle between the sample surface (the

horizontal axis) and the incident beam vector corresponds to the incident angle ω, and the angle between the incident beam vector and the scattered beam vector corresponds to the scattered angle 2θ. Intensity is captured by the end of the scattered beam vector. In this study, the 1D longitudinal scan was used to measure diffuse scattering from the individual Al_2O_3 and TiO_2 layers. In reciprocal space, it measures the scattered intensity along a tilted line from the origin, where the tilt angle from the Q_z axis is equal to the ω offset angle from half of 2θ. The ω offset of the longitudinal scan should be large enough to avoid the strong specular intensity. As the ω offset is typically less than 1 degree, the longitudinal scan characterizes the nearly out-of-plane size distribution of scattering features.
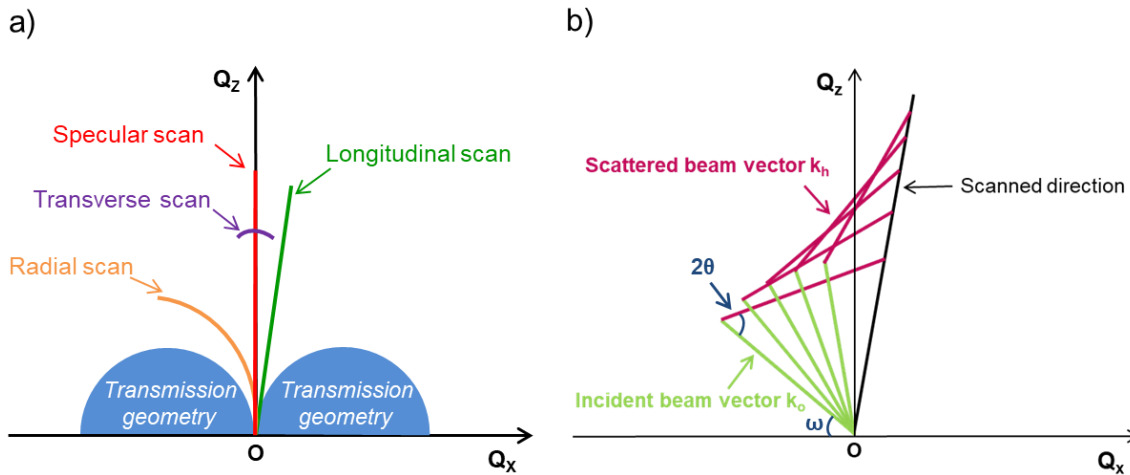
Figure 3.1 – (a) Representations of longitudinal scan, radial scan, transverse scan, and specular scan in reciprocal space. (b) Representation of a scan mode using Ewald sphere construction.

3.2 The Challenge in Prior 1-Dimentional Grazing-Incidence Small Angle X-Ray Scattering Methods

A challenge existing in prior 1D GISAXS methods, however, is separating the diffuse scattering from surface and interface roughnesses and from density fluctuations (e.g. pores) in thin films. As represented in reciprocal space maps in Figure 3.2, they all contribute to total diffuse scattering [65,72]. To accurately determine the pore size distribution from pore scattering, the diffuse scattering from roughnesses needs to be subtracted from the measured total diffuse scattering.
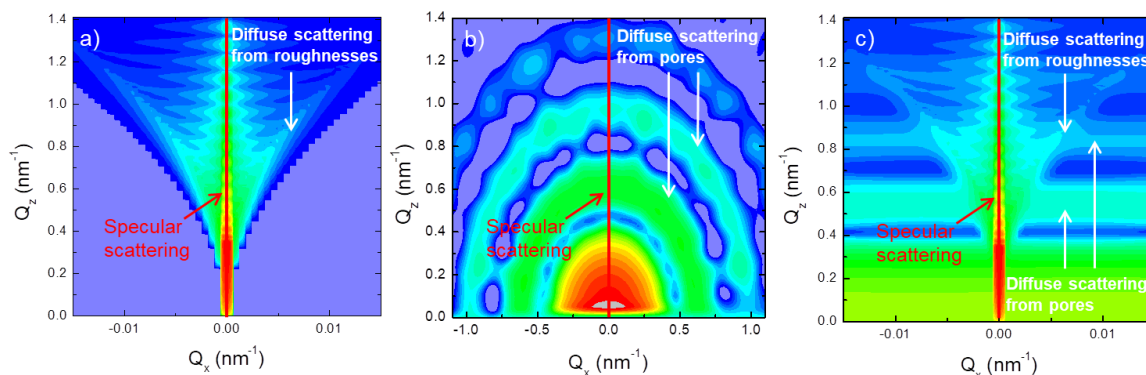
Figure 3.2 – Simulated reciprocal space maps of a 74.0-nm-thick Al_2O_3 layer on a Si substrate with (a) diffuse scattering from vertically correlated surface and interface roughnesses (surface and interface roughnesses are 1.2 nm and 0.7 nm, respectively); (b) pore scattering with a pore diameter of 19 nm; (c) diffuse scattering from both roughnesses and pores.

Theoretically, the diffuse scattering from surface roughness can be calculated with DWBA [73] if surface parameters of root mean square (RMS) roughness σ, lateral correlation length ξ, and Hurst parameter h are known. Simulation indicates diffuse

scattering from interface roughnesses to be negligible as compared to surface roughness. Previously contributions from the roughness and pores were estimated through fitting the sum to both longitudinal and transverse scans [53], and to transverse scans measured at several 2θ positions [52]. However, a challenge associated with these methods is the intercorrelation of a large number of variables in the fitting that may lead to unreal estimations.

3.3 A Combined Approach of Grazing-Incidence Small Angle X-Ray Scattering, Atomic Force Microscopy, and X-Ray Reflectivity

In this study, a new approach combining GISAXS with AFM and XRR is developed. The diffuse scattering from surface roughness is directly estimated with the surface parameters σ, ξ, and h measured by AFM. AFM is a commonly used technique that directly quantifies the surface morphology. It images the surface as a two-dimensional height function Z at discrete points over a finite area. σ can be directly determined with the AFM images. Also, the height-height correlation function (HHCF), g, can be expressed as

$$g(r) = \left\langle \left[Z(\vec{x}) - Z(\vec{x} - \vec{r}) \right]^2 \right\rangle$$

Eq. 3.3

where $\vec{x}$ is any specific point in the image and $\vec{r}$ is a displacement vector. It describes the average of height difference square between any two points separated by a distance r. For most cases, solids, surface and interfaces have self-affine nature such that the height-height correlation function g (r) can be expressed as [73]

$$g(r) = 2\sigma^2 \left[1 - e^{-\left(\frac{r}{\xi}\right)^{2h}} \right]$$

Eq. 3.4

Through least squares fitting maximizing R^2, the surface parameters σ, ξ, and h can be extracted from the experimental HHCF obtained from AFM images. These surface parameters, along with the layer density, the surface grading, and interface roughnesses and/or grading determined by specular XRR simulation, enables one to calculate the diffuse scattering from the roughness with DWBA. Finally, pore scattering can be determined as the intensity difference between the measured total diffuse scattering and the calculated diffuse scattering from the roughness, from which pore size distribution can be obtained using the least squares fitting that minimizes MAE_{log} introduced in Chapter 2. Applications of this combined method of GISAXS, AFM, and XRR include any thin films with surface and interface roughness and/or grading below ~ 5 nm and the density difference between layer and substrate above ~ 10 %, for which the specular XRR measurement works.

3.4 Validation of The Combined Approach of Grazing-Incidence Small Angle X-Ray Scattering, Atomic Force Microscopy, and X-Ray Reflectivity

A porous indium phosphide (InP) layer on bulk InP was characterized for validating this combined approach of GISAXS, AFM, and XRR. It was fabricated through galvanostatic etching in dilute HCl solutions. The plane-view scanning electron microscopy (SEM) image shown in the inset of Figure 3.3 suggests the pore size

distribution displayed in Figure 3.3 with an average diameter of 160 nm and a standard deviation of 24 nm assuming a spherical shape.
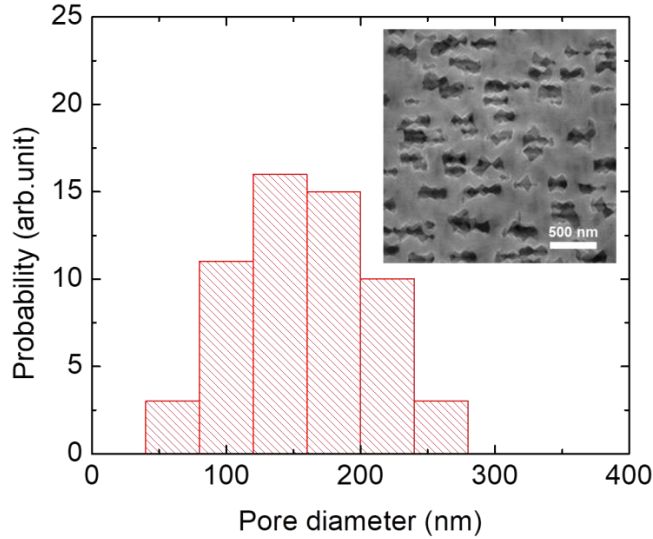
Figure 3.3 – Pore size distribution in the porous InP layer on bulk InP obtained from the plane-view SEM image (Inset).

A surface RMS roughness σ of 2.6 ± 0.5 nm is obtained from AFM images. It was averaged over five 40 μm × 40 μm AFM images with 256 lines × 256 lines, one of which is shown in Figure 3.4 (a). The AFM images were taken in uniformly distributed areas on the sample surface in order to obtain a good statistical average. Figure 3.4 (b) shows the experimental HHCF averaged over five 1 μm × 1 μm AFM images (512 lines × 512 lines) measured in the same areas and the best-fit simulated HHCF (R^2 = 0.998). The experimental HHCF were obtained from AFM images using Gwyddion 2.47 software [74]. The lateral correlation length ξ represents the in-plane feature size of surface morphology. Typically the image size needs to be more than ten times larger than ξ in order to get good statistics, and the number of scan lines should ensure sufficient data

points (~ 8 points) within the in-plane feature size. From the best-fit simulated HHCF, the lateral correlation length ξ 150 ± 20 nm and the Hurst parameter h 0.7 ± 0.1 were determined using a Matlab code. Jordan Valley REFS 4.5 simulation software was used to perform specular XRR simulation obtaining layer densities, surface grading, and interface roughnesses and/or grading, and also to simulate the diffuse scattering from the roughness with the parameters determined from specular XRR and AFM. Equipment settings such as the incident beam size, detector slit size, and distance from sample to detector need to be input in the simulation software. A bare Si wafer was used as the calibrant as it has no pore scattering. The equipment settings were determined through matching the simulated diffuse scattering from surface roughness of Si to the measured total diffuse scattering. Specular XRR simulation suggests the density of the porous InP layer to be 50 ± 3 % of the bulk density. The measured total diffuse scattering and the simulated diffuse scattering from the roughness of the porous InP layer with respect to Q are shown in Figure 3.5. A longitudinal scan with a ω offset of 0.1 degree was performed to measure the total diffuse scattering. The total diffuse scattering higher than the diffuse scattering from roughness suggests the additional scattering from pores in the InP layer. Pore scattering was calculated as the intensity difference between the diffuse scattering from roughness and the total diffuse scattering. It has similar intensity and trend (MAE_{log} = 0.182) with the simulated pore scattering (Scatter 2.5 simulation software [75]) using pore size distribution (Figure 3.3) obtained from the plane-view SEM image (the inset of Figure 3.3). The simulation also suggests the same phenomena for pores assumed with other shapes than spheres. This validates the combined approach of GISAXS, AFM, and XRR in determining the pore size distribution.
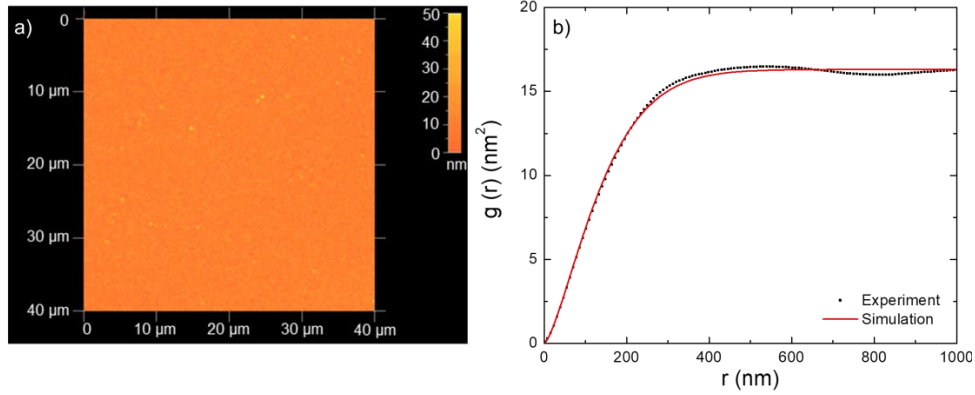
Figure 3.4 – (a) The representative 40 μm × 40 μm AFM image with 256 lines × 256 lines and (b) the experimental and best-fit simulated HHCF g(r) with $R^2 = 0.998$ of the porous InP layer on bulk InP.
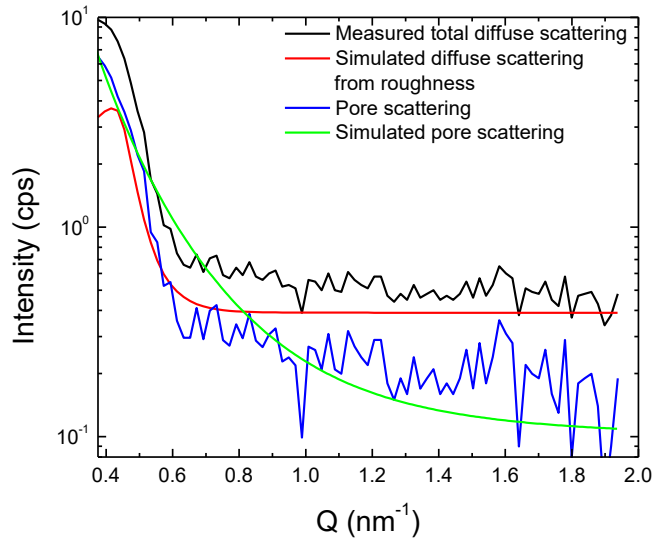
Figure 3.5 – Measured total diffuse scattering and simulated diffuse scattering from roughness of the porous InP layer on bulk InP. ω offset of the longitudinal scan is 0.1 degree. Pore scattering calculated as the intensity difference between measured total diffuse scattering and simulated diffuse scattering from roughness, and simulated pore scattering using pore size distribution suggested by the plane-view SEM image, are also shown.

Chapter 4 Experimental Details

In this study, the multilayer $Al_2O_3/TiO_2/Al_2O_3$ ARC and individual Al_2O_3 and TiO_2 layers were deposited by ALD. Layer thicknesses were measured with the XRR method introduced in Chapter 2 as well as TEM, SE, and spectrophotometry measurements. XRR also characterized layer densities that were correlated with refractive indices obtained from SE and spectrophotometry measurements. The combined approach of GISAXS, AFM, and XRR introduced in Chapter 3 was used to characterize the pore size distribution in the individual Al_2O_3 and TiO_2 layers. Crystal structures of the multilayer ARC and individual layers were accessed by GIXRD, TEM SAED patterns, and HRTEM images. STEM-EDX was used to measure chemical compositions in the multilayer ARC. In the following sections, experimental apparatus for the fabrication and characterization techniques will be described.

4.1 Atomic Layer Deposition

The multilayer $Al_2O_3/TiO_2/Al_2O_3$ ARC and individual Al_2O_3 and TiO_2 layers were deposited using a ULTRATECH (Cambridge NanoTech Fiji F200) ALD system. TMA and H_2O were used as the precursors for Al_2O_3, and Tetrakis(dimethylamino)titanium and H_2O were used as the precursors for TiO_2. Typical thermal ALD parameters were used with a deposition temperature of 200 °C.

4.2 X-Ray Scattering Techniques

The XRR, GISAXS, and GIXRD measurements were performed on a Jordan Valley D1 high-resolution X-ray diffractometer with a Cu sealed tube source. Monochromatic Cu Kα1 radiation was used for the measurements. The diffractometer is

composed of three "parts", also referred to as three "axes". Its schematic representation is shown in Figure 4.1. The first "axis" aims to collimate the X-ray beam from the X-ray tube source with a Maxflux specular mirror and make it monochromatic Cu Kα1 radiation with a Si (220) two reflection collimator crystal. Before incident on the sample, the X-ray beam is defined to be 1 mm in width and 10 mm in height by an incident beam slit. The second "axis" is the sample stage. It controls the sample moving in six-axes: ω axis controlling the incident angle; χ axis controlling sample tilt; φ axis controlling azimuthally rotation; Z axis moving samples in and out of the X-ray beam; X and Y axes moving samples laterally and vertically in the plane perpendicular to the φ axis. The third "axis" consists of a detector, two scattered beam slits, and a Si (220) two reflection analyzer crystal in between the two slits. The Si analyzer crystal can be translated in and out of the beam path. The measurement with Si analyzer crystal in the beam path is referred to as triple axis diffraction (TAD) measurement. In TAD, the Si analyzer crystal defines the acceptance angle to be approximately 0.003 degree (11 arcsec), which enables high-resolution X-ray scattering measurements. On the other hand, the measurement with Si analyzer crystal out of the beam path is referred to as double axis diffraction (DAD) measurements, in which the acceptance angle is determined by the widths of scattered beam slits. The acceptance angle of DAD is on the order of 0.1 degree (360 arcsec) which is much larger than that of TAD. Therefore, DAD has a lower resolution than TAD but receives higher scattered beam intensity. In this study, TAD was used for XRR and GISAXS measurements and DAD was used for GIXRD measurements. Radial scans were performed in GIXRD measurements with an incident angle of 1 degree.
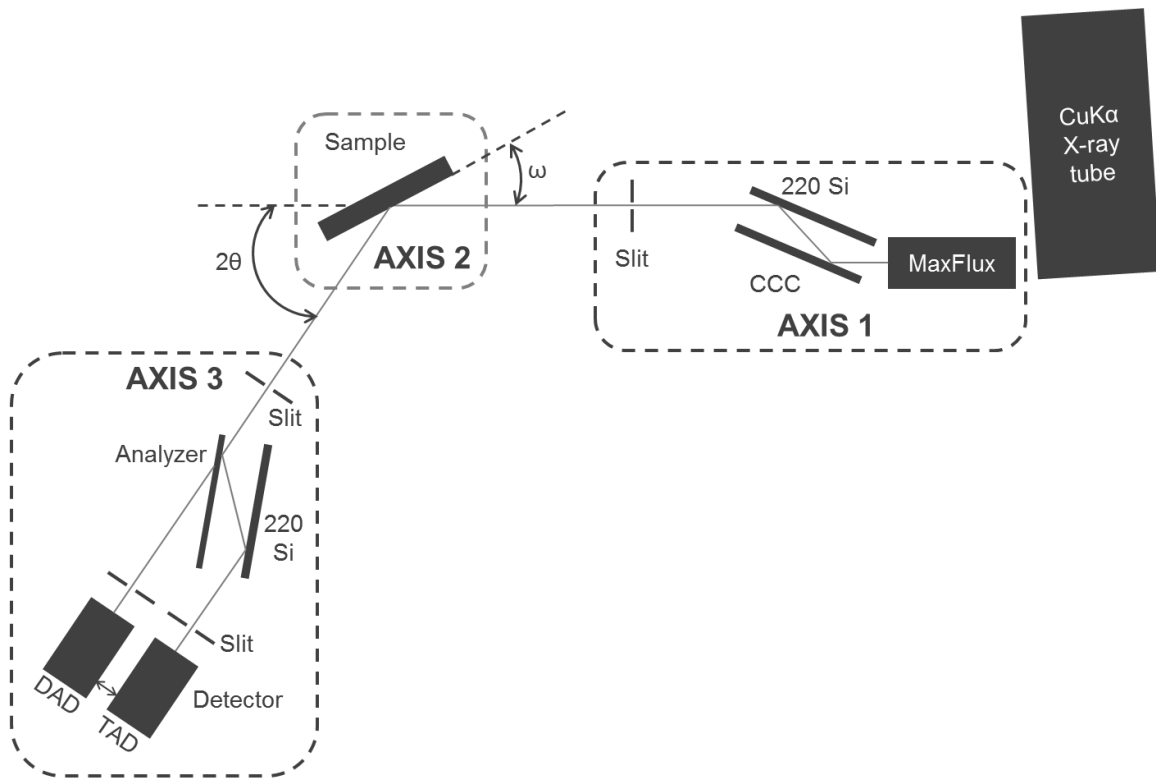
Figure 4.1 – Schematic of Jordan Valley D1 high-resolution X-ray diffractometer.

In addition, AFM measurements were conducted using a Quesant Q250 AFM in tapping mode. A scan rate of 1 Hz was used for all the scans. Surface parameters σ, ξ, and h for the estimation of diffuse scattering from the roughness were determined with the AFM images.

4.3 Spectroscopic Ellipsometry and Spectrophotometry

SE is a non-destructive technique that determines thin film thicknesses with sub-nm precision and dispersion relations of refractive indices. Orthogonally polarized light is used as the incident light in which s wave oscillates perpendicular to the plane of incidence and parallel to the sample surface, and p wave oscillates parallel to the plane of incidence. Phase shift (difference) Delta and amplitude ratio tan (Psi) of complex

reflection coefficients of s and p waves are measured as the incident light reflected on the sample surface. Thicknesses and refractive indices can be obtained through fitting the ellipsometric data with the Levenberg-Marquardt regression method. Since the ratio (or difference) instead of absolute values is measured, ellipsometry is considered as a highly accurate and reproducible technique that is insensitive to intensity variations in the incident beam. Also, reference samples are not needed for ellipsometry measurements.

In this study, a Sopra GES 5 spectroscopic ellipsometer was used. The incident beam has a circular shape with a diameter of approximately 2 mm. The incident angle was kept at 75 degree for all the measurements. The ellipsometric data were measured in the wavelength range from 350 nm to 840 nm. Winelli 4.07 simulation software was used for the Levenberg-Marquardt regression through which layer thicknesses and refractive indices were obtained from the measured data.

A SCI FilmTek 2000 spectrophotometer was used for optical reflectance measurements. The incident beam is circular with a diameter of approximately 3 mm. Optical transmittance was measured by a Hitachi U-4100 UV-Vis-NIR spectrophotometer, with a circular beam approximately 2 mm in diameter. Both optical reflectance and transmittance were measured under normal incidence within the same wavelength range as ellipsometry. Layer thicknesses and refractive indices were obtained through simulations using a Mathcad code.

4.4   Transmission Electron Microscopy

TEM directly reveals layer thicknesses, crystal structures, and surface and interface roughnesses of thin films. The incident electron beam with a narrow energy and angular divergence is produced by an electron gun and condenser lenses. As it penetrates

through the thin sample with a thickness of approximately 100 nm, both elastic and inelastic scattering occurs, during which energy spread and angular distribution are produced. The scattered electron beam is finally recorded by a CCD camera. There are three basic contrast mechanisms at least one of which contributes to the contrast in a TEM image. The mass contrast occurs for all materials. It is the major contrast for non-crystalline materials. Thicker and denser regions of the specimen scatter more and appear darker on the image, while thinner or lighter regions scatter less and appear brighter. The second contrast mechanism is the diffraction contrast which occurs only for crystalline materials. It stems from the diffraction induced by atomic periodicity in the crystal. An objective aperture is typically added to the back focal plane of objective lens to select either the transmitted beam or one of the diffracted beams to pass through and form the final image. If the objective aperture is centered about the optical axis, the transmitted beam is selected, which forms a bright field image. Layer thicknesses and surface and interface roughnesses of multilayer systems can be revealed by bright field images. On the other hand, a dark field image is obtained if the objective aperture selects one of the diffracted beams to pass through. Only grains contributing to the selected diffraction appear bright while the other areas show a dark background. The diffraction pattern and dark field images can be used to assess crystallization in thin films. Another contrast in TEM images is the phase contrast, through which high-resolution TEM (HRTEM) imaging is realized. Atoms in the actual crystal can be observed in HRTEM images, which is achieved due to the phase difference of the transmitted beam and multiple diffracted beams within the aligned zone axis. HRTEM is a powerful technique that directly reveals the crystallization in thin films.

In addition, a scanning coil can be added to the TEM system that enables the STEM mode. The STEM mode focuses the incident beam to a narrow spot which scans over the sample. Combined with EDX, it enables to measure chemical compositions along 1D profiles and in 2D maps. For a multilayer system, layer compositions can be assessed with STEM-EDX measurements on the cross-section of the multilayers.

In this study, an FEI Titan S/TEM with an accelerating voltage of 300 kV was used for the TEM and STEM-EDX measurements. Cross-section samples of multilayer ARCs were extracted with a NOVA 600 Focused Ion Beam Tool via a Ga+ source. In order to protect the sample from damages by the scattered ion beam during sample thinning, Pt protection layers were deposited on sample surfaces.

Chapter 5 Layer Properties of Individual Al_2O_3 and TiO_2 Layers on Si

The Al_2O_3/TiO_2/Al_2O_3 multilayer ARC deposited by ALD is a good candidate for that on the III-V space multi-junction solar cells. In order to assess optical properties of the multilayer ARC and the effects of optimization methods, it is necessary to characterize layer properties of the individual Al_2O_3 and TiO_2 layers. Refractive indices of the individual layers will be used for designing the multilayer ARC. The individual Al_2O_3 and TiO_2 layers were deposited on Si substrates and characterized with the XRR method discussed in Chapter 2, the combined method of GISAXS, AFM and XRR introduced in Chapter 3, SE, optical reflectance, and GIXRD. Influences of post-annealing at 400 °C for 10 min and 40 min in air and varying ALD parameters on the layer properties were revealed.

5.1 TiO_2 Layer on Si

5.1.1 As-Deposited TiO_2 Layer on Si

Both experimental and best-fit simulation ($MAE_{log} = 0.023$) specular XRR data of the as-deposited TiO_2 film on Si are shown in Figure 5.1 (a). Contrast fringes of the specular data attest to the density difference between the TiO_2 layer and the Si substrate. Figure 5.1 (b) shows DFT power spectrum of the processed experimental data with the multiplication of Q_z^4 and differentiation [49], based on which the XRR simulation model was built. Only one peak emerges that corresponds to the thickness of TiO_2. The DFT power spectrum determines a thickness of 41.2 ± 0.2 nm that agrees well with 41.4 ± 0.1 nm obtained from the best-fit specular XRR simulation. This demonstrates the

effectiveness of the DFT algorithm in layer thickness determination. The thickness value from the specular XRR simulation also coincides with 41.7 ± 0.3 nm from both SE and optical reflectance measurements. Besides, an interfacial layer between the TiO_2 layer and Si substrate is suggested, with which a better fit to the SE and optical reflectance data was obtained. It is not revealed by specular XRR probably due to a small density difference (on the order of a few percent) from the Si substrate. Distinct to specular XRR is the determination of layer densities. A density of 3.96 g/cm^3 for the as-deposited TiO_2 is determined by specular XRR with an uncertainty less than one percent. Meanwhile, the absence of diffraction peaks in the GIXRD data displayed in Figure 5.2 suggests an amorphous structure of the TiO_2 layer. The layer density determined by specular XRR is larger than the literature value of amorphous TiO_2 (3.8 g/cm^3) [76] and also close to bulk TiO_2 (4.23 g/cm^3).
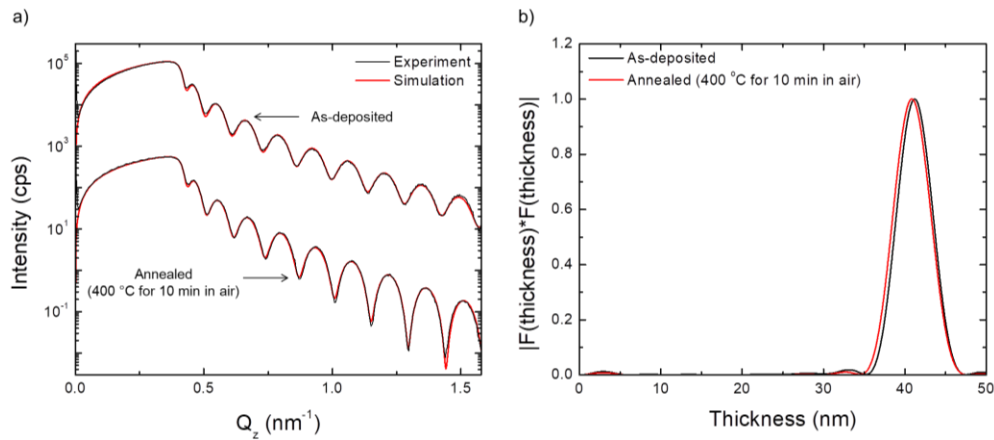
Figure 5.1 – Specular XRR measurements of the as-deposited and the annealed (400 °C for 10 min in air) TiO_2 layers on Si substrates: (a) experimental and best-fit simulation specular XRR data. The curves are offset for clarity. MAE_{log} for the as-deposited and the annealed (400 °C for 10 min in air) TiO_2 layers are 0.023 and 0.033, respectively. (b) DFT power spectrum of the experimental specular XRR data.
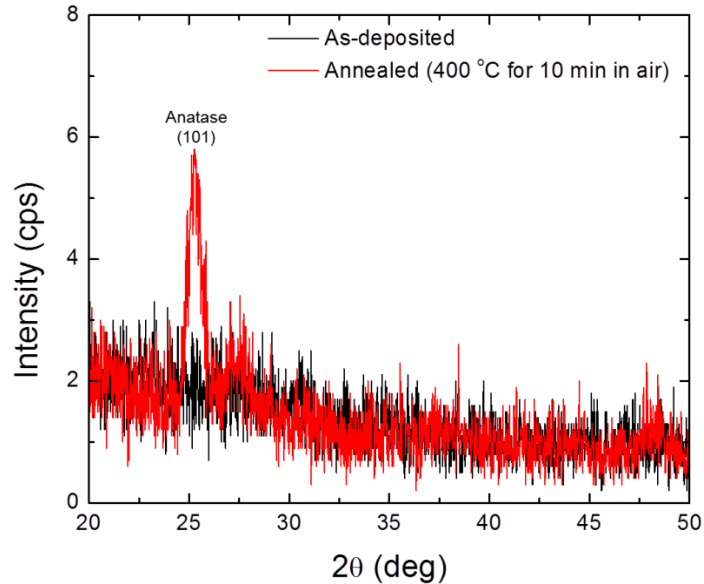
Figure 5.2 – GIXRD data of the as-deposited and the annealed (400 °C for 10 min in air) TiO$_2$ layers on Si substrates. The incident angle ω is 1 degree.

Figure 5.3 shows the measured total diffuse scattering and the simulated diffuse scattering from roughness of the as-deposited TiO$_2$ layer on Si. The diffuse scattering from roughness was simulated using 0.4 ± 0.1 nm, 30.0 ± 10.0 nm, and 0.6 ± 0.1 of surface parameters σ, ξ, and h determined by AFM together with the layer density and surface and interface roughness and grading characteristics determined by specular XRR simulation. A ω offset of 0.3 degree was used for the longitudinal scan. The total diffuse scattering and the diffuse scattering from roughness show negligible intensity difference within the range of noise, which suggests the absence of additional scattering such as that related to the presence of pores.

44
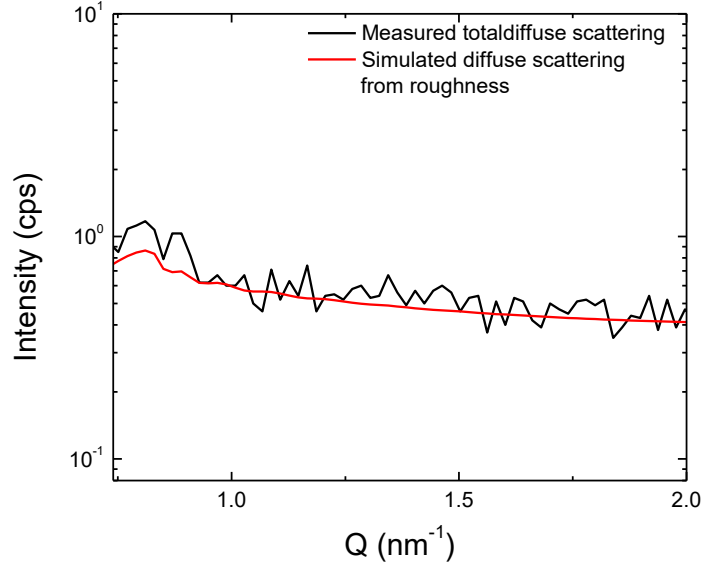
Figure 5.3 – Measured total diffuse scattering and simulated diffuse scattering from roughness of the as-deposited TiO_2 layer on a Si substrate. ω offset of the longitudinal scan is 0.3 degree.

5.1.2 Annealed TiO_2 Layer on Si

The experimental and best-fit simulation ($MAE_{log} = 0.033$) specular XRR data of the annealed TiO_2 layer at 400 °C for 10 min in air are also shown in Figure 5.1 (a). They are vertically transferred for comparison. A 1.1 % decrease in the layer thickness after annealing is determined by specular XRR simulation, which agrees with the decrease in layer thickness revealed by the DFT power spectrum in Figure 5.1 (b). Also, specular XRR simulation determines a 1.8 % density increase in TiO_2 after annealing, which is suggested by the larger amplitude of fringes in the specular XRR pattern corresponding to an increased density contrast between the TiO_2 layer and the Si substrate. The densification of TiO_2 is probably due to the initiated crystallization indicated by the presence of (101) anatase peak in the GIXRD data shown in Figure 5.2. In addition, the

refractive index of the annealed TiO_2 layer increases slightly as determined by SE and optical reflectance measurements. This suggests a good correlation between the refractive index and the density.

5.2 Al_2O_3 Layer on Si

5.2.1   As-Deposited Al_2O_3 Layer on Si

Figure 5.4 shows both experimental and best-fit simulation (MAE_{log} = 0.092) specular XRR data of the as-deposited Al_2O_3 film on Si. Specular XRR simulation determines the Al_2O_3 layer thickness of 74.3 ± 0.2 nm lower than 76.8 ± 0.3 nm obtained from SE and optical reflectance measurements. This could be attributed to the formation of an interfacial layer that has a similar refractive index with the Al_2O_3 layer and a similar density with the Si substrate. Amorphous structure of the Al_2O_3 layer is suggested by GIXRD data with the absence of diffraction peaks. The density 2.94 g/cm^3 determined by specular XRR simulation is lower than the literature value of amorphous ALD Al_2O_3 (3.15 g/cm^3) [18] and much less than bulk value (3.97 g/cm^3), indicating the as-deposited Al_2O_3 layer to be porous, non-stoichiometric, and/or incorporated with hydrogen species.
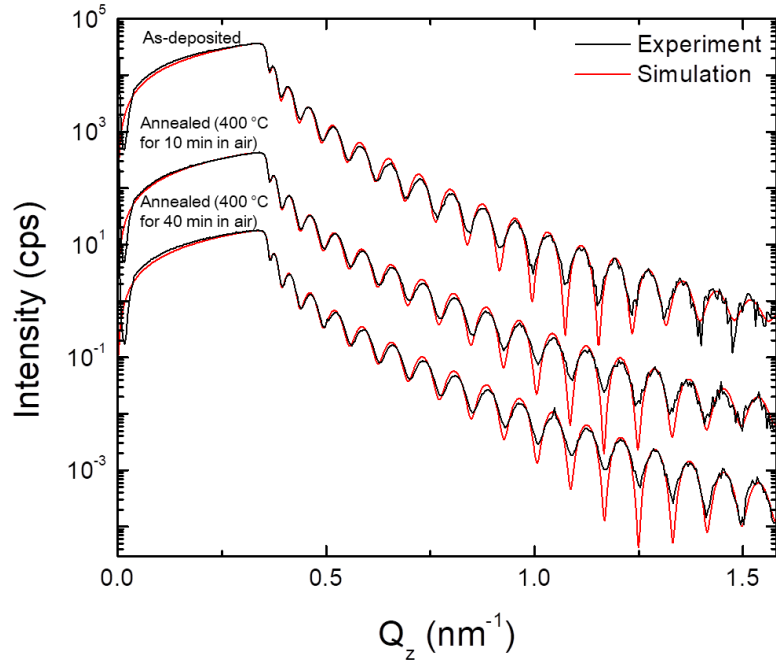
Figure 5.4 – Experimental and best-fit simulation specular XRR data of the as-deposited and the annealed (400 °C for 10 min and 40 min in air) Al_2O_3 layers on Si substrates. The curves are offset for clarity. MAE_{log} for the as-deposited and the annealed (400 °C for 10 min and 40 min in air) Al_2O_3 layers are 0.092, 0.094 and 0.095, respectively.

Figure 5.5 shows the measured total diffuse scattering and the simulated diffuse scattering from roughness of the Al_2O_3 layer on Si. The intensity of total diffuse scattering higher than the scattering from roughness suggests pore scattering in the Al_2O_3 layer. Figure 5.6 shows the pore size distribution obtained from the best-fit simulated pore scattering ($MAE_{log} = 0.079$). An average pore size of 14.0 nm along the out-of-plane direction is determined with an uncertainty of $\sim \pm 2.0$ nm.
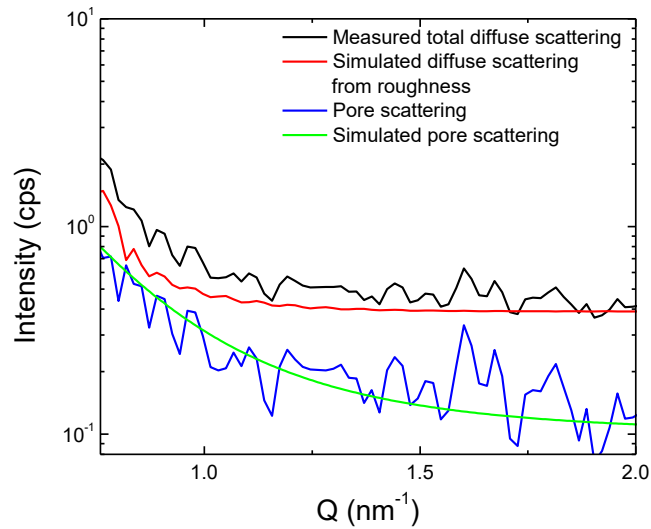
Figure 5.5 – Measured total diffuse scattering and simulated diffuse scattering from roughness of the as-deposited Al_2O_3 layer on a Si substrate. ω offset of the longitudinal scan is 0.3 degree. Pore scattering calculated as the intensity difference between measured total diffuse scattering and simulated diffuse scattering from roughness, and the best-fit simulated pore scattering ($MAE_{log} = 0.079$), are also shown.
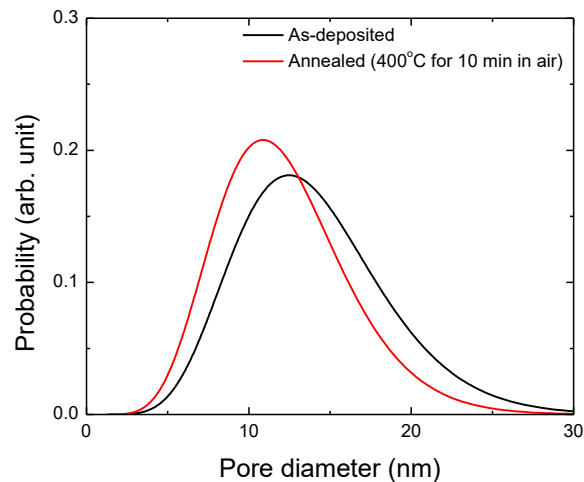
Figure 5.6 – Pore size distributions of the as-deposited and the annealed (400 °C for 10 min in air) Al_2O_3 layers on Si substrates.

In order to validate the combined method of GISAXS, AFM, and XRR developed in this study and also assess the overall shapes and sizes of pores, a 2D GISAXS measurement with a synchrotron source (Beamline 1-5 of Stanford Synchrotron Radiation Lightsource, SLAC National Accelerator Laboratory) was conducted for the as-deposited Al_2O_3 layer on Si. The 2D GISAXS data is shown in Figure 5.7 (a). Both specular scattering and diffuse scattering from roughnesses and pores are included in a stripe centered at the Q_z axis with a width of $\sim 2\pi/\xi$ (0.003 nm^{-1} for the as-deposited Al_2O_3 on Si with a lateral correlation length of 2200 nm) along Q_y, while the scattering intensity further away from the Q_z axis outside the stripe arises from pore scattering. The variation in pore scattering with respect to Q along the Q_z direction provides the out-of-plane pore size information while that along the Q_y direction provides the in-plane pore size information. Due to the weak pore scattering intensity, averaged intensity within 5-degree-wide sectors in the 2D GISAXS data is used to determine pore size distribution along different directions. The sectors are centered along tilted lines with different offset angle α from the Q_z axis. Figure 5.7 (b) shows the experimental sector averaged pore scattering and the best-fit simulation from which the pore size distribution is extracted as shown in Figure 5.7 (c). The sector averaged pore scattering with different α angles is vertically offset for comparison. An average pore size of $\sim$ 14 nm along the out-of-plane direction is suggested by the pore size distribution with α of 5 degree, which is consistent with the result from the combined method of GISAXS, AFM, and XRR. In addition, the average pore size decreases with α, suggesting an elongated pore shape (e.g. ellipsoid or cuboid) along the out-of-plane direction. An average pore size of $\sim$ 2 nm in the in-plane direction is estimated through the pore size distribution with different α angles.
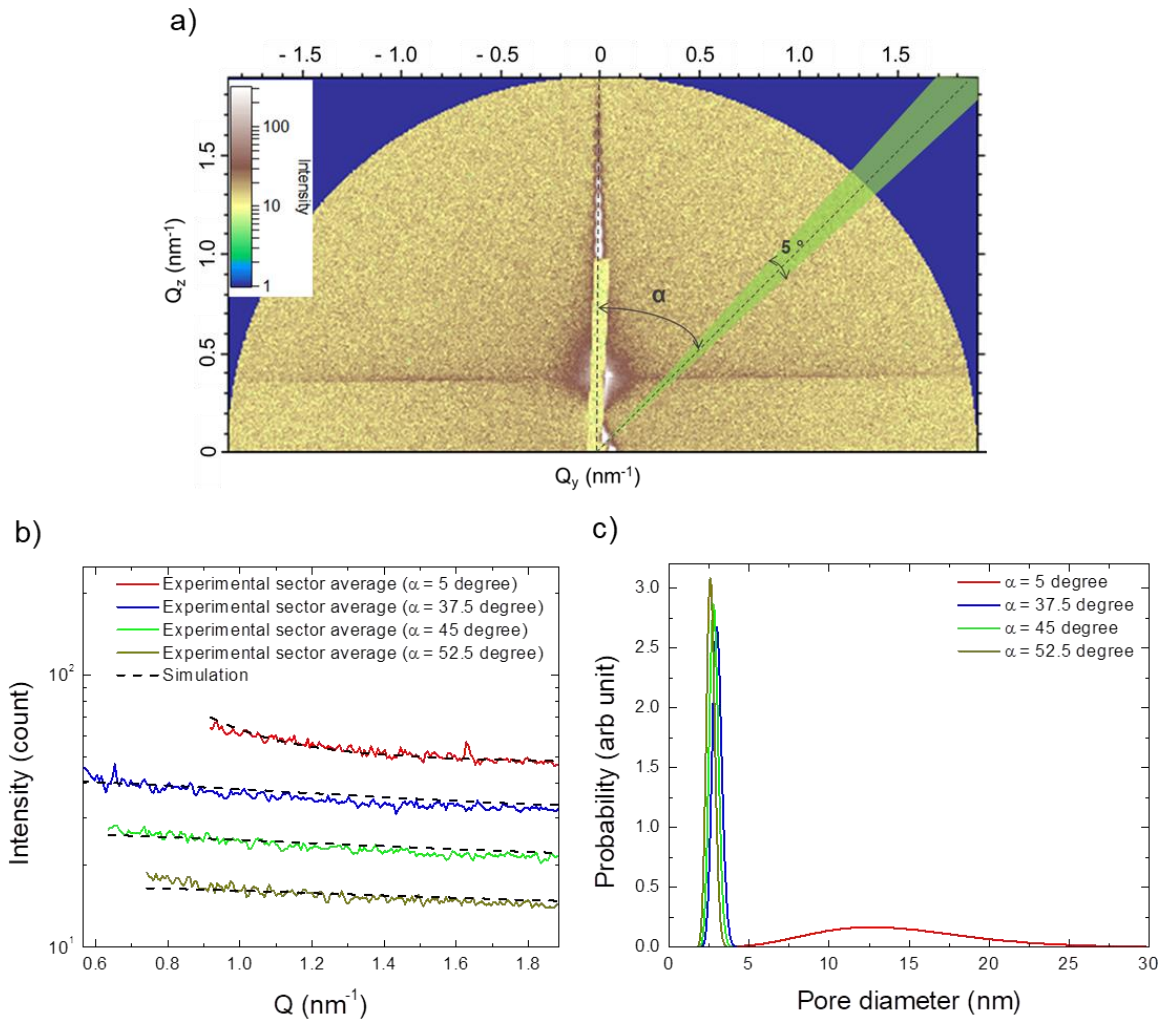
Figure 5.7 – (a) 2D GISAXS data, (b) sector averaged pore scattering from the 2D GISAXS in (a) and best-fit simulated pore scattering, and (c) pore size distribution of the as-deposited Al_2O_3 layer on a Si substrate. The green area in (a) represents a sector in which the pore scattering is averaged. The sector averaged pore scattering with different α angles in (b) is vertically offset for comparison.

5.2.2 Annealed Al_2O_3 Layer on Si

The experimental and best-fit simulation specular XRR data of the annealed Al_2O_3 layer at 400 °C for 10 min and 40 min in air are also shown in Figure 5.4. They are

vertically transferred for comparison. MAE_{log} of annealed Al_2O_3 layers for 10 min and 40 min are 0.094 and 0.095, respectively. After annealing at 400 °C for 10 min in air, the Al_2O_3 layer has a slight density increase (less than one percent) as determined by specular XRR simulation while remaining amorphous as suggested by GIXRD. The combined approach of GISAXS, AFM, and XRR also reveals the existence of pores and a slight decrease in pore sizes as shown in Figure 5.6. This is probably attributed to diffusion from the bulk material into the pores. The shrinking of pores along with the loss of hydrogen from hydroxyl groups initially present in the Al_2O_3 layer [46] could account for the slight densification of the Al_2O_3 layer. To further determine the effect of annealing, the Al_2O_3 layer was annealed at 400 °C in air for 40 min. After annealing, it is still amorphous as suggested by GIXRD. Figure 5.8 shows negligible intensity difference between the total diffuse scattering and the diffuse scattering from roughness, indicating the disappearance of pores in Al_2O_3. This could be attributed to diffusion into the pores as well. Meanwhile, specular XRR suggests a slight density increase in the Al_2O_3 layer annealed for the longer time, which could be associated with the disappearance of pores and the loss of hydrogen from hydroxyl groups [46].
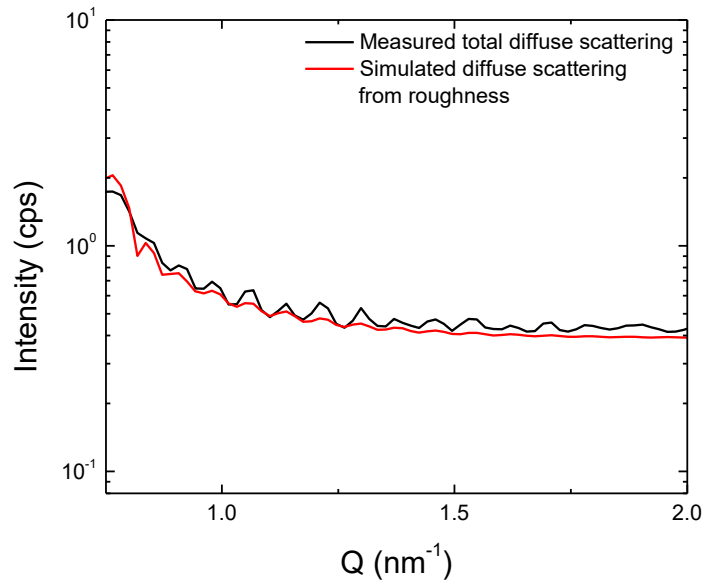
Figure 5.8 – Measured total diffuse scattering and simulated diffuse scattering from roughness of the annealed (400 °C for 40 min in air) Al_2O_3 layer on a Si substrate. ω offset of the longitudinal scan is 0.3 degree.

5.2.3 As-Deposited Al_2O_3 Layer on Si with Varied Atomic Layer Deposition Parameters

The measured total diffuse scattering and the simulated diffuse scattering from roughness of an Al_2O_3 layer with varied ALD parameters (referred to as Al_2O_3 #2 below) are shown in Figure 5.9. As compared to the Al_2O_3 layer with original ALD parameters (referred to as Al_2O_3 #1 below), the difference between the measured total diffuse scattering and the simulated diffuse scattering from roughness is negligible within the range of noise, which indicates the absence of pore scattering in Al_2O_3 #2. Figure 5.10 shows the 2D GISAXS data and the sector averaged pore scattering of Al_2O_3 #2 as well as the sector averaged pore scattering of Al_2O_3 #1 for comparison. The nearly flat sector

averaged pore scattering of Al_2O_3 #2 with respect to Q as compared to that of Al_2O_3 #1 suggests the absence of pore scattering (or a small pore size less than ~ 2 nm) in Al_2O_3 #2, which is consistent with the result from the combined approach of GISAXS, AFM and XRR developed in this study. In addition, specular XRR simulation determines a higher density 3.01 g/cm^3 of Al_2O_3 #2 than 2.94 g/cm^3 of Al_2O_3 #1. This could be correlated with the pores in Al_2O_3 #1 while the absence of pores in Al_2O_3 #2. Besides, optical reflectance and SE measurements reveal a higher refractive index ($\lambda = 550$ nm) of Al_2O_3 #2 (1.649 ± 0.003) than Al_2O_3 #1 (1.629 ± 0.003), which is consistent with the higher density of Al_2O_3 #2 and also agrees with the results from the combined approach of GISAXS, AFM, and XRR and the 2D GIDAXS measurement.
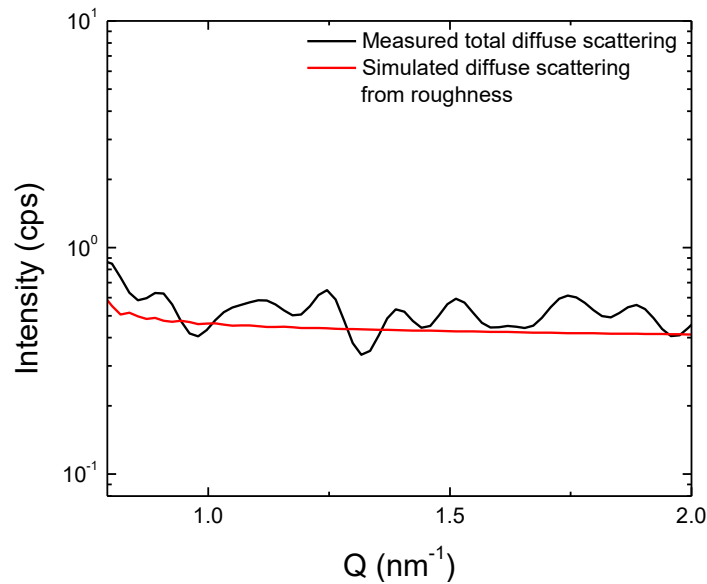
Figure 5.9 – Measured total diffuse scattering and simulated diffuse scattering from roughness of the as-deposited Al_2O_3 layer on a Si substrate with varied ALD parameters. ω offset of the longitudinal scan is 0.3 degree.
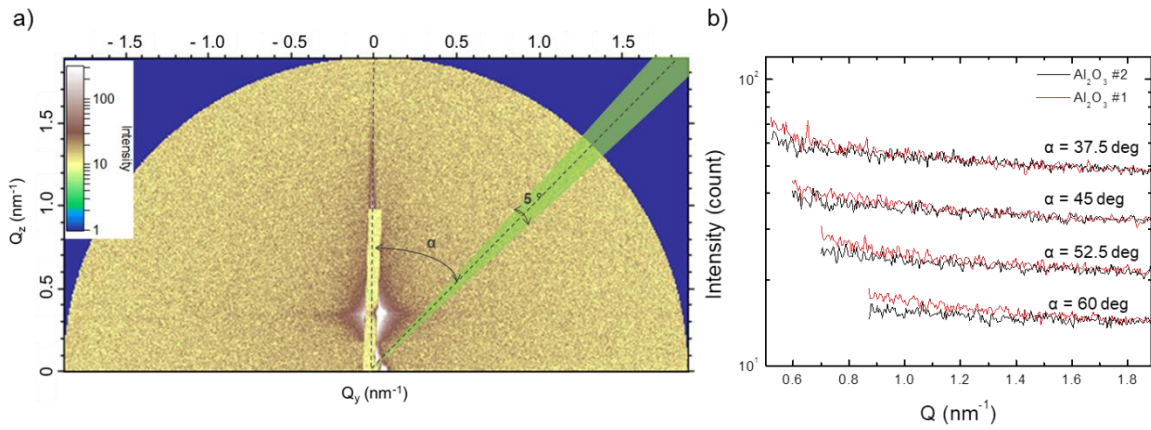
Figure 5.10 – (a) 2D GISAXS data of the as-deposited Al_2O_3 layer on a Si substrate with varied ALD parameters. (b) Sector averaged pore scattering from the 2D GISAXS in (a) along with that of the as-deposited Al_2O_3 layer on a Si substrate with original ALD parameters. The green area in (a) represents a sector in which the pore scattering is averaged. The sector averaged pore scattering with different α angles in (b) is vertically offset.

Chapter 6 Optical Properties of Multilayer Al$_2$O$_3$/TiO$_2$/Al$_2$O$_3$ Antireflection Coatings on Si

In order to demonstrate the ability to deposit the multilayer Al$_2$O$_3$/TiO$_2$/Al$_2$O$_3$ ARC by ALD and determine the effects of optimization methods on the optical properties, the multilayer Al$_2$O$_3$/TiO$_2$/Al$_2$O$_3$ ARC was deposited on a Si substrate with the same ALD parameters as the individual TiO$_2$ and Al$_2$O$_3$ (original parameters) layers on Si. Optical properties of the multilayer Al$_2$O$_3$/TiO$_2$/Al$_2$O$_3$ ARC were characterized by the XRR method discussed in Chapter 2, SE, optical reflectance, GIXRD, and TEM measurements of BFTEM, SAED, HRTEM, and STEM-EDX. The effect of annealing at 400 °C for 10 min in air on optical properties of the multilayer Al$_2$O$_3$/TiO$_2$/Al$_2$O$_3$ ARC was revealed.

6.1 Designing of Multilayer Al$_2$O$_3$/TiO$_2$/Al$_2$O$_3$ Antireflection Coating

Target thicknesses of 76.8 nm, 37.1 nm, and 5.5 nm for the top Al$_2$O$_3$ layer, the middle TiO$_2$ layer, and the bottom Al$_2$O$_3$ layer were determined with the SWR minimized using refractive indices of individual TiO$_2$ and Al$_2$O$_3$ layers. The schematic graph of the target multilayer Al$_2$O$_3$/TiO$_2$/Al$_2$O$_3$ ARC is shown in Figure 6.1. The n values of ARC layers correspond to the wavelength of 550 nm.
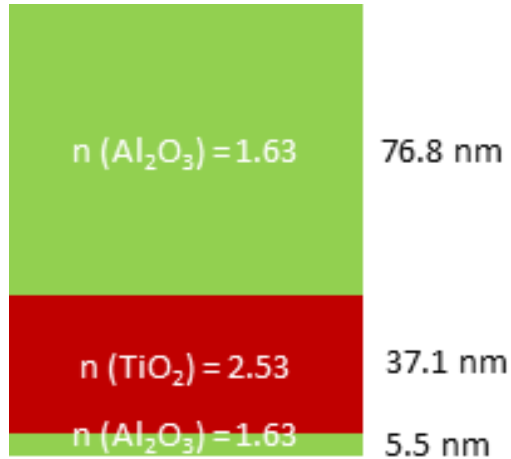
Figure 6.1 – Schematic graph of the target multilayer $Al_2O_3/TiO_2/Al_2O_3$ antireflection coating designed for an inverted metamorphic 4-junction space solar cell. The n values correspond to the wavelength of 550 nm.

6.2 As-Deposited Multilayer $Al_2O_3/TiO_2/Al_2O_3$ Antireflection Coating on Si

Figure 6.2 (a) shows the experimental and best-fit simulation (MAE_{log} = 0.080) specular XRR data of the as-deposited $Al_2O_3/TiO_2/Al_2O_3$ multilayer ARC on Si. Interference fringes in the XRR pattern are formed with scattered beams from multiple ARC layers and the Si substrate with different densities. Figure 6.3 shows the DFT power spectrum of the experimental data processed with the multiplication of Q_z^4 and differentiation [49], based on which the XRR simulation model was built. The DFT power peaks are associated with thicknesses of either individual or multiple ARC layers. For example, Peak t_1 originates from the middle TiO_2, and Peak t_4 represents the combination of the top Al_2O_3 and the middle TiO_2. Layer thicknesses obtained from the DFT power spectrum are also shown in Figure 6.2 (b). They agree well with those

56

obtained from the best-fit XRR simulation listed Table 6.1. This demonstrates the extreme effectiveness of this novel DFT algorithm for multilayer ARCs. Table 6.1 also displays measured thicknesses from the cross-sectional BFTEM image shown in Figure 6.3 and SE and optical reflectance measurements besides the XRR simulation. A good agreement is achieved among thicknesses obtained from different techniques, which validates the XRR method. In addition, the BFTEM image shows flat ARC layers parallel to the substrate surface, which is consistent with the surface and interface roughnesses and/or grading on the order of 1.0 nm determined by XRR.
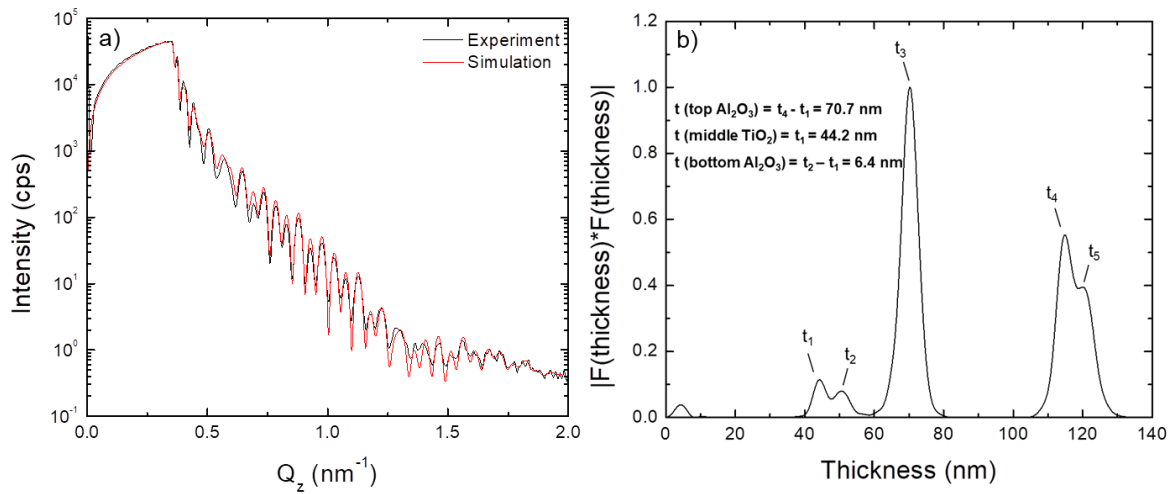
Figure 6.2 – Specular XRR measurement of the multilayer $Al_2O_3/TiO_2/Al_2O_3$ antireflection coating on a Si substrate: (a) experimental and best-fit simulation (MAE_{log} = 0.080) specular XRR data. (b) DFT power spectrum of the experimental specular XRR data.
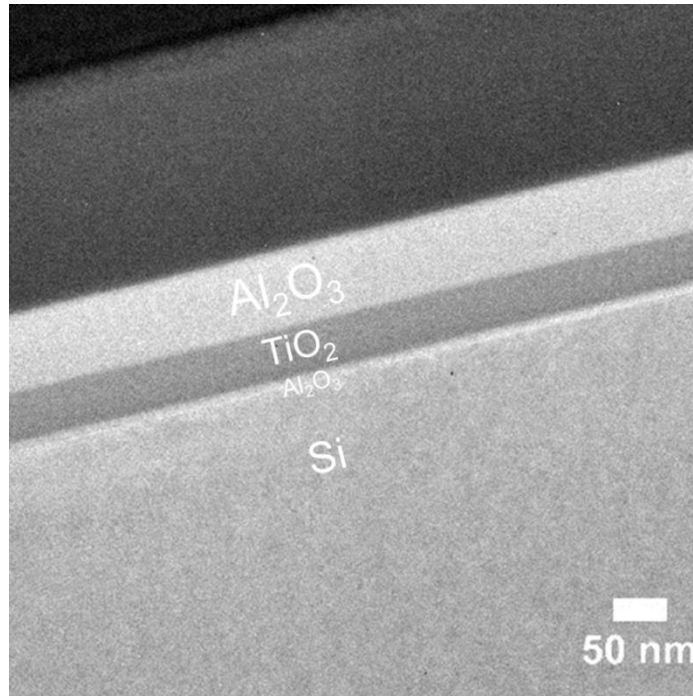
Figure 6.3 – Cross-sectional BFTEM image of the as-deposited multilayer $Al_2O_3/TiO_2/Al_2O_3$ antireflection coating on a Si substrate.

TABLE 6.1 Thickness values of the as-deposited $Al_2O_3/TiO_2/Al_2O_3$ multilayer stack on a Si substrate.

	XRR (nm)	SE, optical reflectance (nm)	BFTEM (nm)
Al_2O_3	70.5	70.0	70.0
TiO_2	43.7	43.7	45.0
Al_2O_3	7.3	6.8	7.0

Amorphous TiO_2 and Al_2O_3 layers in the as-deposited multilayer ARC are indicated by the TEM SAED pattern displayed in Figure 6.4 (a) which shows only the Si diffraction pattern. It is also supported by the GIXRD data shown in Figure 6.4 (c) with

the absence of diffraction peaks. The TiO_2 density 3.47 g/cm^3 determined by the XRR method is smaller than the literature value of amorphous TiO_2 (3.80 g/cm^3) [76] and much smaller than the bulk value (4.23 g/cm^3). This suggests the TiO_2 layer to be porous, non-stoichiometric, and/or incorporated with hydrogen-containing species. On the other hand, XRR determines densities of 3.01 g/cm^3 and 2.80 g/cm^3 for the top and bottom Al_2O_3 layers, respectively, which is consistent with the higher refractive index of the top Al_2O_3 layer than the bottom Al_2O_3 layer obtained from SE and optical reflectance measurements. The lower densities than the literature value of amorphous Al_2O_3 (3.15 g/cm^3) [18] and the bulk value (3.97 g/cm^3) could be due to the pores, non-stoichiometry, and/or hydrogen-containing species in Al_2O_3 layers as well.
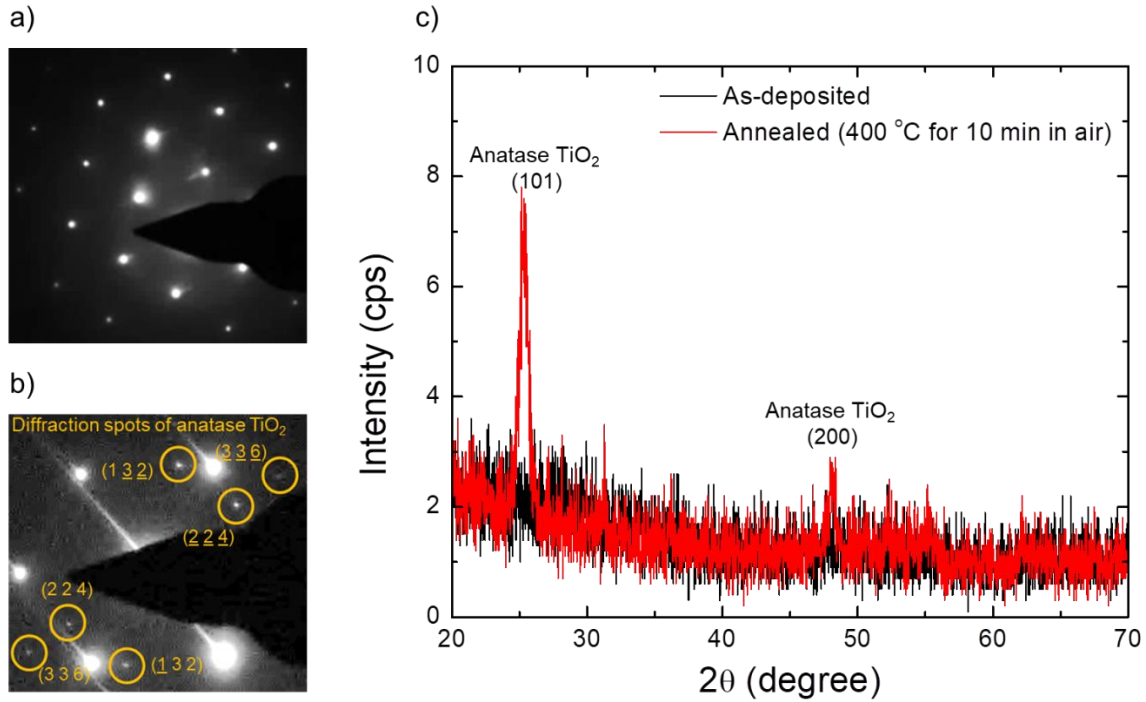
Figure 6.4 – TEM SAED pattern of (a) the as-deposited multilayer $Al_2O_3/TiO_2/Al_2O_3$ antireflection coating on a Si substrate and (b) the annealed (400 °C for 10 min in air) multilayer $Al_2O_3/TiO_2/Al_2O_3$ antireflection coating on a Si substrate. The TEM SAED patterns were measured on the cross-section of both the multilayer $Al_2O_3/TiO_2/Al_2O_3$ antireflection coating and the Si substrate. Only Si diffraction pattern shows up for the as-deposited multilayer $Al_2O_3/TiO_2/Al_2O_3$ antireflection coating on Si while diffraction patterns of both anatase TiO_2 (marked by yellow circles) and Si show up for the annealed (400 °C for 10 min in air) multilayer $Al_2O_3/TiO_2/Al_2O_3$ antireflection coating on Si. (c) GIXRD data of the as-deposited and the annealed (400 °C for 10 min in air) multilayer $Al_2O_3/TiO_2/Al_2O_3$ antireflection coatings on Si substrates. The incident angle ω is 1 degree.

6.3 Annealed Multilayer Al$_2$O$_3$/TiO$_2$/Al$_2$O$_3$ Antireflection Coating on Si

The multilayer Al$_2$O$_3$/TiO$_2$/Al$_2$O$_3$ ARC was annealed at 400 °C for 10 min in air in order to determine the effect of annealing on the optical properties. The experimental and best-fit simulation (MAE$_{log}$ = 0.079) specular XRR data of the annealed multilayer ARC are also shown in Figure 6.5. The best-fit XRR simulation determines a 10.1 % density increase in the annealed TiO$_2$ layer. This could be attributed to the initiated crystallization in TiO$_2$, which is suggested by the GIXRD data shown in Figure 6.4 (c) with the presence of (101) and (200) anatase peaks, and also confirmed by the presence of anatase diffraction spots in the TEM SAED pattern shown Figure 6.4 (b) and the crystallized areas in HRTEM images shown Figure 6.6. On the other hand, no evidence suggests crystallization in the annealed Al$_2$O$_3$ layers. XRR determines a 0.6 % decrease in the thickness of the top Al$_2$O$_3$ layer and a 5.5 % increase in that of the bottom Al$_2$O$_3$ layer.
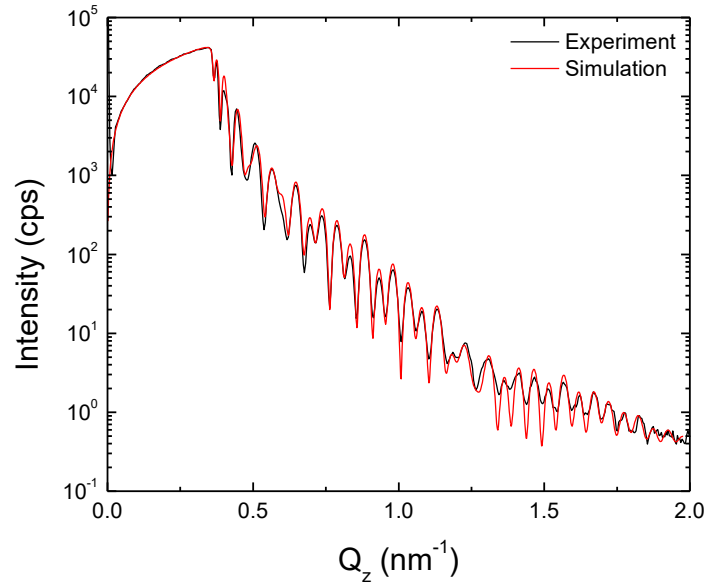
Figure 6.5 – Experimental and best-fit simulation ($MAE_{log} = 0.079$) specular XRR data of the annealed (400 °C for 10 min and 40 min in air) multilayer $Al_2O_3/TiO_2/Al_2O_3$ antireflection coatings on a Si substrate.
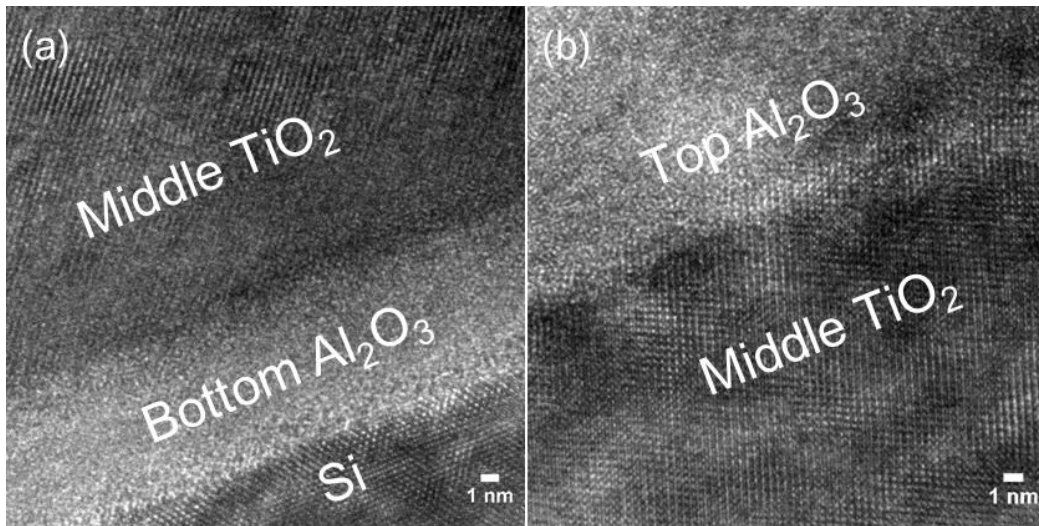
Figure 6.6 – HRTEM images of the annealed (400 °C for 10 min in air) multilayer $Al_2O_3/TiO_2/Al_2O_3$ antireflection coating on a Si substrate.

Figure 6.7 (a) shows cross-sectional STEM-high-angle annular dark-field (STEM-HAADF) images of both as-deposited and annealed multilayer stacks. The Al_2O_3 layers appear dark and the TiO_2 layer appears bright in STEM-HAADF images. STEM-EDX composition maps shown in Figure 6.7 (b) were taken within the areas represented by the white rectangles. To better reveal composition changes along the out-of-plane direction of the multilayer ARC, composition line profiles averaged along the Y axis at different X positions in Figure 6.7 (a) are shown in Figure 6.7 (c). As indicated by composition maps and line profiles of Al and Ti, annealing induces interdiffusion of Al and Ti between the top Al_2O_3 layer and the middle TiO_2 layer. The interdiffusion, as well as the loss of hydrogen from hydroxyl groups initially present in the ALD layers [46], could account for the 0.6 % thickness decrease in the top Al_2O_3 layer. Also, it is shown in the composition map and line profile of Si that substrate Si atoms diffuse into all the ALD layers after annealing. This could cause the thickness increase in the bottom Al_2O_3 layer after annealing with a Si volume fraction of 5.5 % or less in the bottom layer. The phenomenon of Si diffusion into the ALD Al_2O_3 layer was also reported by Cho et al. [77] In addition, silicide and SiO_2 could form in the middle TiO_2 layer due to the possible chemical reaction between TiO_2 and Si diffusing from the substrate [78]. Considering the annealed TiO_2 layer to be composed of amorphous TiO_2, crystallized TiO_2, silicide, and SiO_2, the crystallized TiO_2 is estimated to be ~ 63 % of the annealed TiO_2 layer using the thickness and density values determined by XRR simulation.
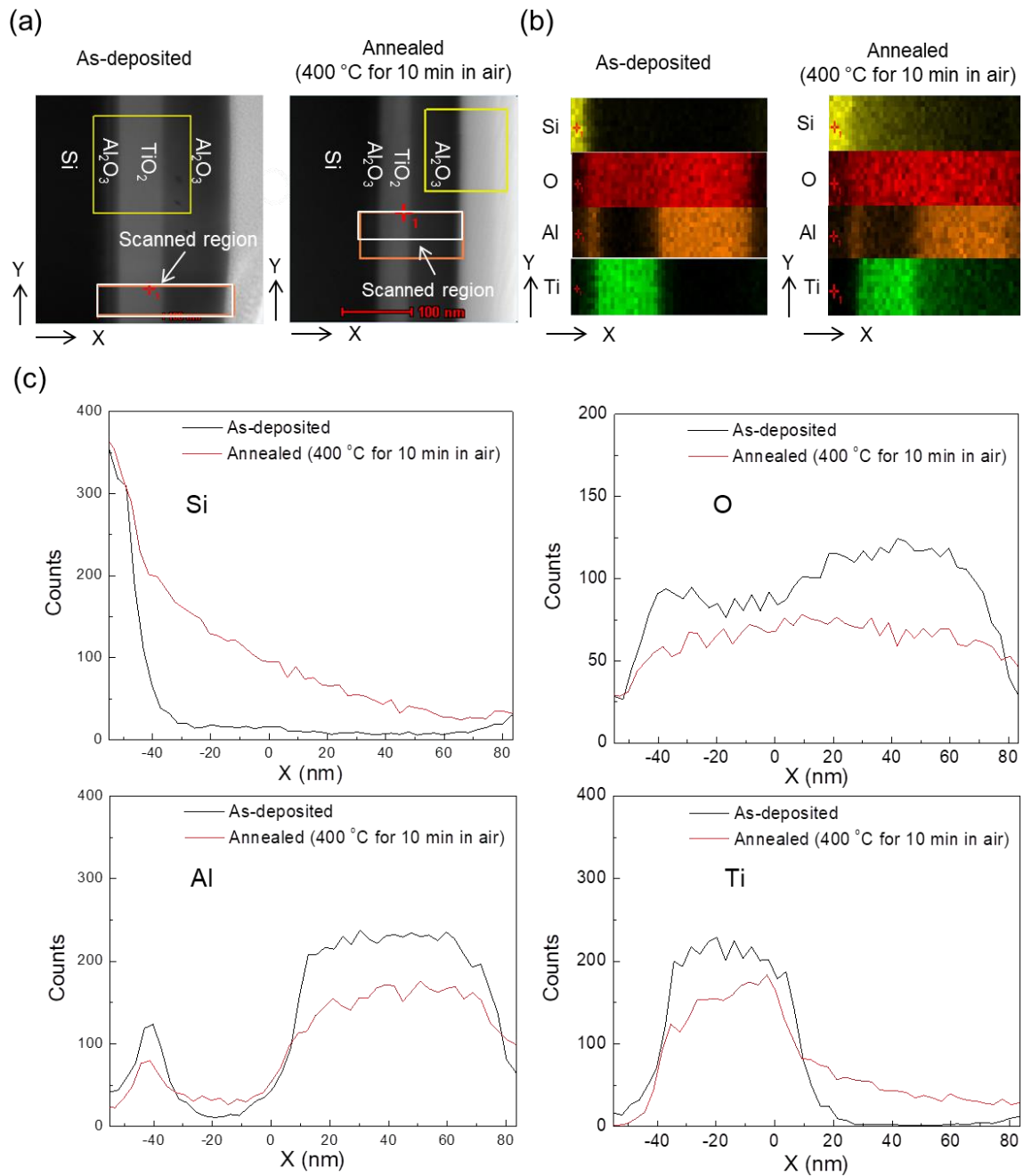
Figure 6.7 – (a) STEM-HAADF images of the as-deposited and the annealed (400 °C for 10 min in air) multilayer $Al_2O_3/TiO_2/Al_2O_3$ antireflection coatings on Si substrates; (b) Composition maps of Si, O, Al and Ti in the regions of white rectangles in STEM-HAADF images; (c) Composition profiles extracted from the composition maps of Si, O, Al and Ti.

Chapter 7 Optical Properties of Multilayer $Al_2O_3/TiO_2/Al_2O_3$ Antireflection Coatings on III-V Substrates

This chapter presents the assessment of the actual optical performance of the multilayer $Al_2O_3/TiO_2/Al_2O_3$ ARC on the III-V multi-junction solar cell. The multilayer $Al_2O_3/TiO_2/Al_2O_3$ ARC with the same target thicknesses and refractive indices introduced in Chapter 6 and the same ALD parameters as the individual TiO_2 and Al_2O_3 (original parameters) layers on Si was deposited on a III-V substrate including lattice-matched AlInP (30 nm) / GaInP (100 nm) layers on a GaAs substrate. AlInP and GaInP are typically the window layer and the top sub-cell as the topmost layers in III-V multi-junction solar cells. Optical reflectance of the multilayer ARC was characterized and compared to the target spectrum. Besides, layer properties of the multilayer ARC were also characterized by the XRR method discussed in Chapter 2, SE, GIXRD, and TEM measurements of BFTEM, SAED, and HRTEM. In addition, the optical transmittance of the same multilayer $Al_2O_3/TiO_2/Al_2O_3$ ARC deposited on an AlInP (30 nm) / sapphire substrate was measured in order to assess internal scattering in ARC layers. The internal scattering was also revealed by the combined method of GISAXS, AFM, and XRR introduced in Chapter 3.

7.1 Multilayer $Al_2O_3/TiO_2/Al_2O_3$ Antireflection Coating on AlInP (30 nm) / GaInP (100 nm) / GaAs

The lattice-matched AlInP (30 nm) / GaInP (100 nm) layers were grown on a (001) oriented GaAs substrate by molecular beam epitaxy (MBE). Figure 7.1 (a) shows the experimental and best-fit simulation (MAE_{log} = 0.100) specular XRR data of the $Al_2O_3/TiO_2/Al_2O_3$ multilayer ARC on the AlInP (30 nm) / GaInP (100 nm) / GaAs substrate. Interference fringes in the XRR pattern are formed with reflections from multiple ARC layers, III-V layers, and the GaAs substrate that have different densities. Figure 7.1 (b) shows the DFT power spectrum of the experimental data processed with the multiplication of Q_z^4 and differentiation [49], based on which the XRR simulation model was built. The DFT power peaks are associated with thicknesses of individual and multiple ARC layers and III-V layers. For example, Peak t_4 originates from the top Al_2O_3 layer, and Peak t_7 and t_8 represent sums of ARC layers and III-V layers, respectively. Layer thicknesses of ARC layers and III-V layers obtained from the DFT power spectrum are also shown in Figure 7.1 (b). A good agreement is achieved between the values from the DFT power spectrum and those from the best-fit XRR simulation listed in Table 7.1, suggesting the extreme effectiveness of this novel DFT algorithm for multilayer systems with different kinds of layers. Table 7.1 also displays measured thicknesses from the BFTEM image shown in Figure 7.2 and measured refractive indices from SE, as well as the target values. The XRR method is validated by BFTEM with the consistent thickness values obtained from these two techniques.   Compare with the target thicknesses, the measured values of the middle TiO_2 and the bottom Al_2O_3 are quite close with deviations

less than 2.5 nm while a large discrepancy of ~ 15 nm occurs for the top Al_2O_3 probably due to the inconsistency in the ALD equipment. On the other hand, very close refractive indices to the target values are obtained for the ARC layers. The BFTEM image (Figure 7.2) also shows very flat ARC layers and III-V layers parallel to the substrate surface, which is consistent with the surface and interface roughnesses and/or grading less than 1.0 nm as suggested by XRR simulation and the well-defined thickness fringes in a high-resolution X-ray ω:2θ scan around the GaAs (004) peak.
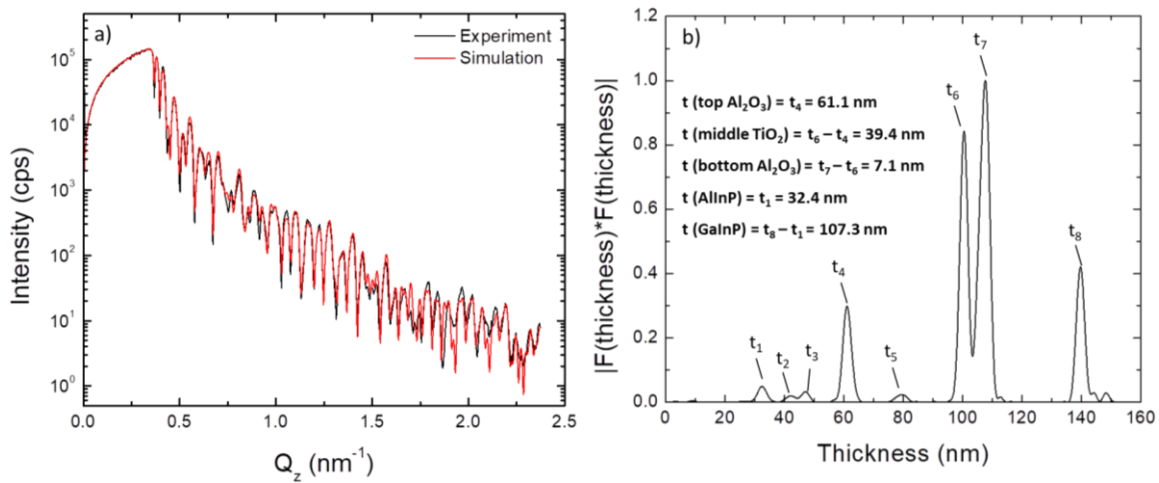
Figure 7.1 – Specular XRR measurement of the multilayer Al_2O_3/TiO_2/Al_2O_3 antireflection coating on an AlInP (30 nm) / GaInP (100 nm) / GaAs substrate: (a) experimental and best-fit simulation (MAE_{log} = 0.100) specular XRR data. (b) DFT power spectrum of the experimental specular XRR data.
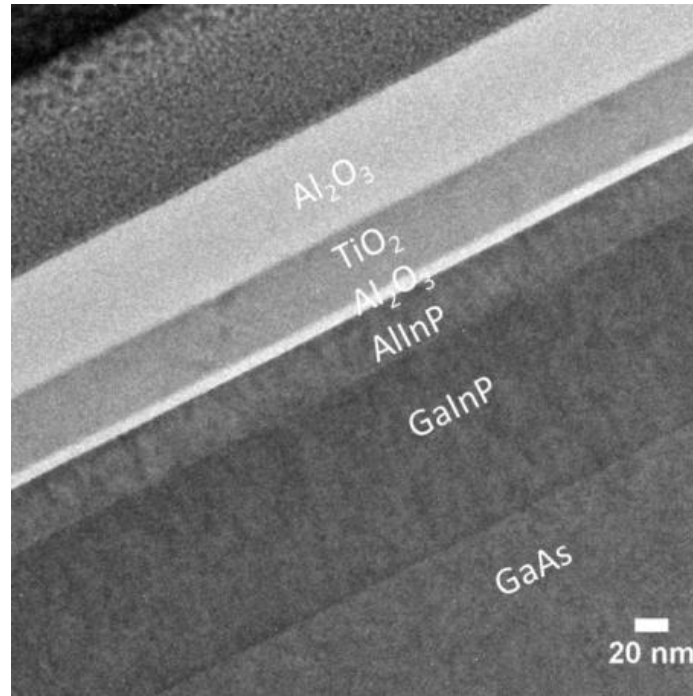
Figure 7.2 – Cross-sectional BFTEM image of the multilayer $Al_2O_3/TiO_2/Al_2O_3$ antireflection coating on an AlInP (30 nm) / GaInP (100 nm) / GaAs substrate.

TABLE 7.1 Thickness and refractive index values of $Al_2O_3/TiO_2/Al_2O_3$ multilayer stack on an AlInP (30 nm) / GaInP (100 nm) / GaAs substrate.

	Thicknesses (nm)			Refractive index	
	Target	XRR	BFTEM	Target	SE
Al_2O_3	76.8	61.4	61.0	1.629	1.636
TiO_2	37.1	38.9	39.0	2.520	2.521
Al_2O_3	5.5	7.7	7.0	1.629	1.635
AlInP	30	32.0	32.0	---	---
GaInP	100	106.8	111.0	---	---

Initiated crystallization in the TiO_2 layer is indicated by the GIXRD data shown in Figure 7.3 (a) with the presence of (101) and (103) anatase peaks. This is also confirmed by the TEM SAED pattern displayed in Figure 7.3 (b) showing diffraction spots of anatase phase (marked by yellow circles) other than III-V layers and HRTEM images displayed in Figure 7.3 (c) and (d) showing crystallized areas (highlighted by yellow contours). The TiO_2 density 4.00 g/cm^3 determined by specular XRR is higher than the literature value of amorphous TiO_2 (3.80 g/cm^3) [76] and close to the bulk TiO_2 (4.23 g/cm^3), which could be correlated with the initiated crystallization. On the other hand, no evidence suggests the crystallization in Al_2O_3 layers.
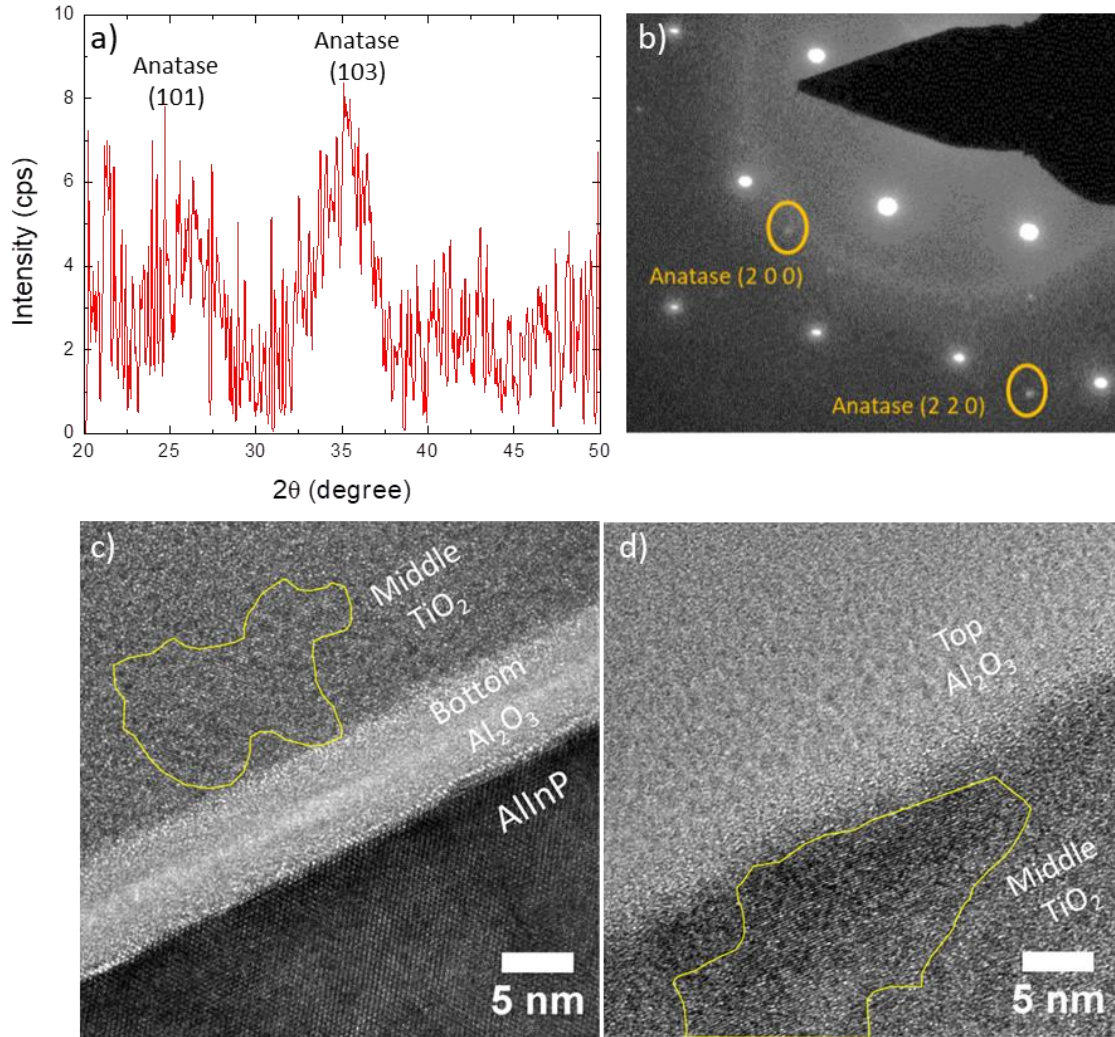
Figure 7.3 – (a) GIXRD data, (b) TEM SAED pattern, and (c) and (d) HRTEM images of the multilayer $Al_2O_3/TiO_2/Al_2O_3$ antireflection coating on an AlInP (30 nm) / GaInP (100 nm) / GaAs substrate. The incident angle ω is 1 degree for the GIXRD measurement. The TEM SAED pattern was measured on the cross-section of both the as-deposited multilayer $Al_2O_3/TiO_2/Al_2O_3$ antireflection coating and the III-V layers of the substrate. Diffraction patterns of both anatase TiO_2 (marked by yellow circles) and III-V layers show up. Highlighted areas by yellow contours in HRTEM images are the crystallized regions in the middle TiO_2 layer.

Figure 7.4 shows the measured optical reflectance of the multilayer $Al_2O_3/TiO_2/Al_2O_3$ ARC and the target optical reflectance. A broadband low reflectance less than 5 % is achieved within 450 – 810 nm that is nearly the whole spectrum absorbed by the current limiting sub-cell 2 of IMM4JSC. Also, a minimum of ~ 2 % is obtained throughout the range of 550 – 750 nm. The discrepancy between the measured and target optical reflectance is mainly due to the deviation of top Al_2O_3 thickness from the target value as suggested by simulation. Corresponding to the measured optical reflectance, J_{SC} and SWR are determined to be 15.3 mA/cm^2 and 2.7 % that are close to the target values of 15.6 mA/cm^2 and 1.4 % as well as the J_{SC} of 15.8 mA/cm^2 with 100 % optical transmittance.
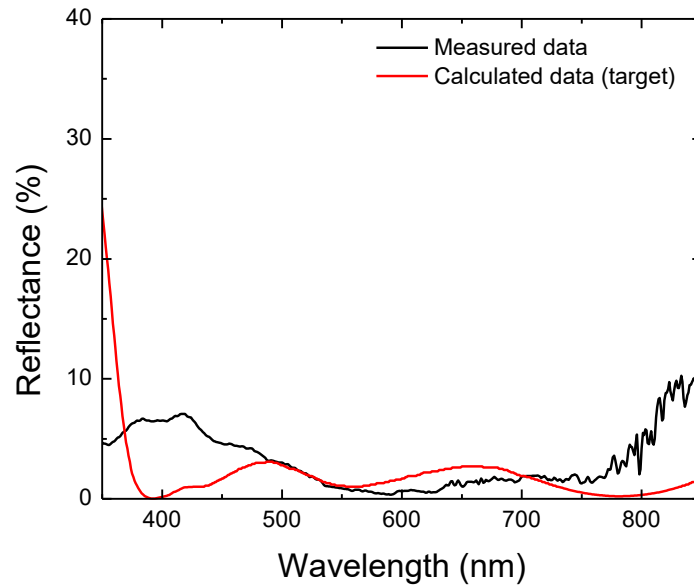
Figure 7.4 – Measured and calculated (target) optical reflectance of the multilayer $Al_2O_3/TiO_2/Al_2O_3$ ARC on an AlInP (30 nm) / GaInP (100 nm) / GaAs substrate.

7.2 Multilayer Al$_2$O$_3$/TiO$_2$/Al$_2$O$_3$ Antireflection Coating on AlInP (30 nm) / Sapphire

The 30-nm-thick AlInP layer was grown on a (0001) oriented sapphire wafer by MBE. It is highly (111) textured as indicated by an X-ray 2θ:ω scan and a rocking curve across the AlInP (111) peak. Surface and interface roughnesses and/or grading of the multilayer Al$_2$O$_3$/TiO$_2$/Al$_2$O$_3$ ARC deposited on the AlInP (30 nm) / sapphire substrate less than 3 nm is suggested by specular XRR simulation. Figure 7.5 shows the measured and calculated optical transmittance of the multilayer Al$_2$O$_3$/TiO$_2$/Al$_2$O$_3$ ARC on AlInP (30nm) / sapphire. The optical transmittance is calculated using layer thicknesses and refractive indices determined from the optical reflectance measurement. Internal scattering is included in the measured data while not in the calculated data. The calculated transmittance higher than the measured transmittance within the spectrum range of 400 – 800 nm suggests the presence of internal scattering. In order to assess internal scattering in the individual Al$_2$O$_3$, TiO$_2$, and AlInP layers, the optical transmittance was also measured for the individual layers deposited on sapphire substrates shown in Figure 7.5. The calculated transmittance higher than the measured transmittance suggests the presence of internal scattering in the TiO$_2$ layer, while the calculated transmittance matching the measured transmittance suggests the absence of internal scattering in Al$_2$O$_3$ and AlInP layers. The internal scattering in TiO$_2$ could be due to the crystallization as the crystallized regions acting as refractive index fluctuations with respect to the amorphous regions. A combination of Rayleigh scattering from the small grains (size < ~ 35 nm) and Mie scattering from the large grains (size > ~ 35 nm)

could occur as suggested by the deviation from the linear relationship between ln(T (%)/100) (T represents optical transmission) and λ^{-4} which is characteristic of Rayleigh scattering while T is independent of λ for Mie scattering. The scattering from the crystallized regions in TiO_2 is also revealed by the combined method of GISAXS, AFM, and XRR. As shown in Figure 7.6 (a), an intensity difference exists between the measured total diffuse scattering and the simulated scattering from the roughness, suggesting additional scattering from density fluctuations related to crystallization in the TiO_2 layer. On the other hand, Figure 7.6 (b) and (c) show nearly no intensity difference between the measured total diffuse scattering and the simulated diffuse scattering from the roughness for the individual Al_2O_3 and AlInP layers on sapphire substrates, which could be correlated with the absence of internal scattering indicated by the optical transmittance measurements.
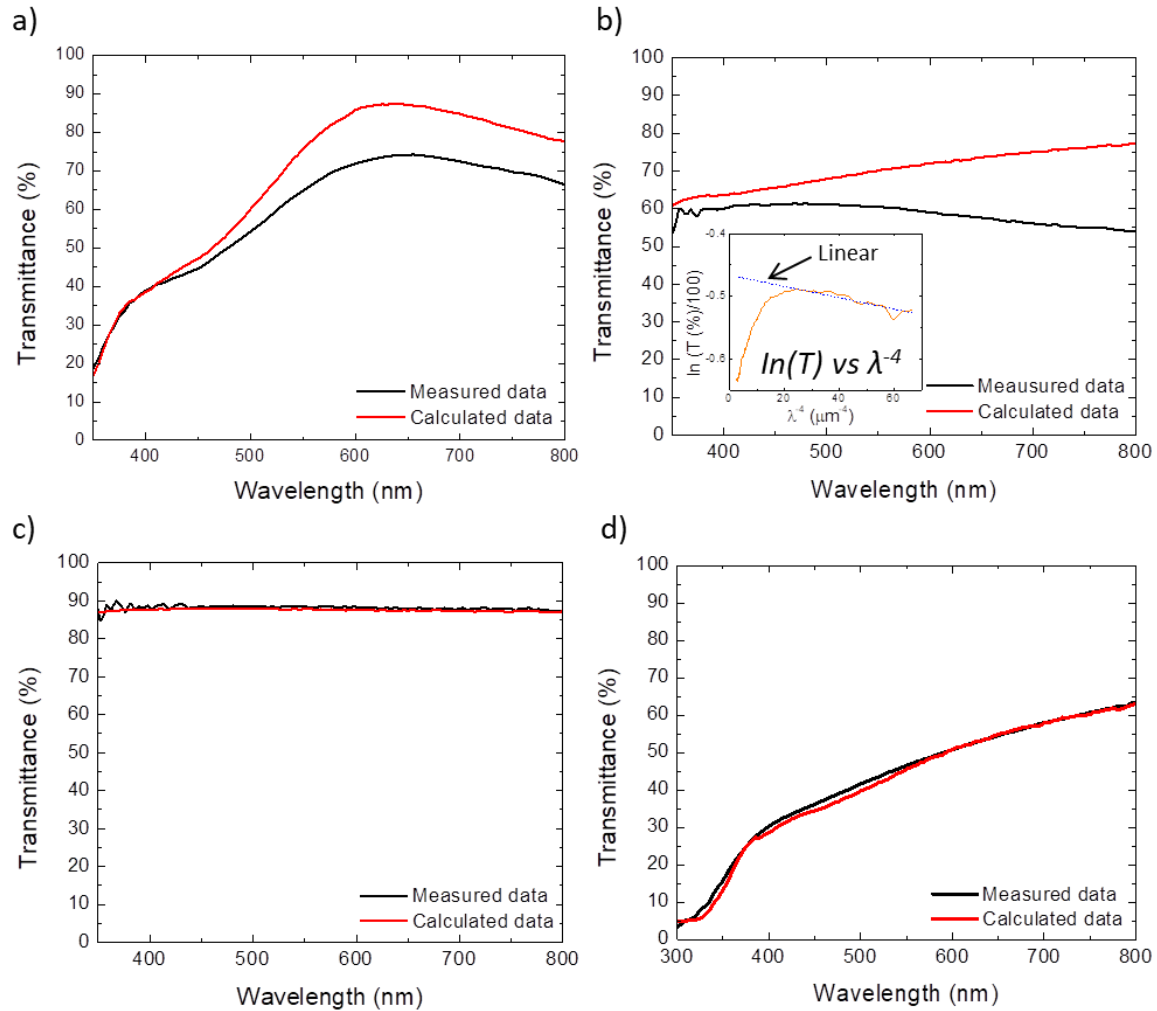
Figure 7.5 – Measured (internal scattering included) and calculated (internal scattering not included) optical transmittance of (a) multilayer $Al_2O_3/TiO_2/Al_2O_3$ ARC on an AlInP (30 nm) / sapphire substrate; (b) individual TiO_2 layer on a sapphire substrate. The inset: $ln(T (\%)/100)$ versus λ^{-4}. (c) individual Al_2O_3 layer on a sapphire substrate; (d) individual AlInP layer on a sapphire substrate.
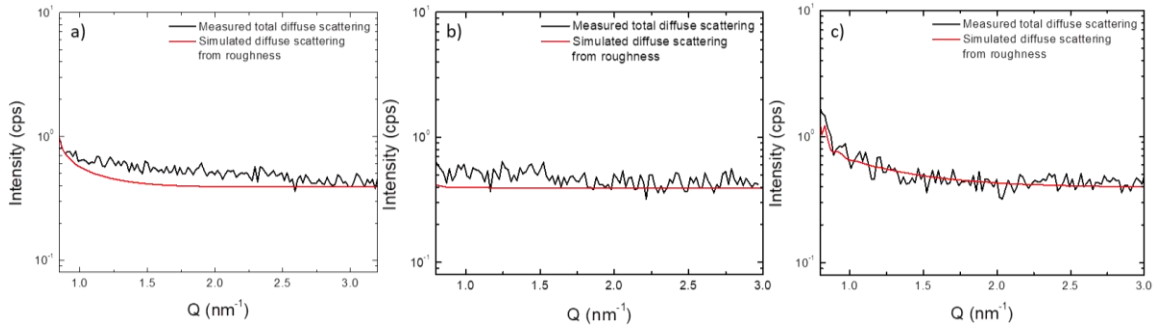
Figure 7.6 – Measured total diffuse scattering and simulated diffuse scattering from roughness (a) individual TiO$_2$ layer on a sapphire substrate; (b) individual Al$_2$O$_3$ layer on a sapphire substrate; (c) individual AlInP layer on a sapphire substrate. ω offset of the longitudinal scans is 0.3 degree.

Chapter 8 Conclusion and Future Work

8.1 Conclusion

This study assesses the optical performance of an ALD multilayer Al_2O_3/TiO_2/Al_2O_3 ARC designed for an IMM4JSC. Layer thicknesses, densities and pore size distributions of the multilayer ARC and the individual Al_2O_3 and TiO_2 layers are determined with X-ray scattering methods including an XRR method combining XRR simulation with a layer thickness extraction algorithm and a combined method of GISAXS, AFM, and XRR developed in this study. Consistent results are obtained from these X-ray scattering techniques as well as other techniques including SE, optical reflectance and transmittance, TEM, STEM-EDX, and GIXRD which also validated the X-ray scattering methods.

Individual Al_2O_3 and TiO_2 layers deposited by ALD have amorphous structures. The as-deposited TiO_2 is non-porous with a density of 3.96 g/cm^3 while the as-deposited Al_2O_3 is porous with a density of 2.94 g/cm^3. The pore size in Al_2O_3 has an average of 14 nm along the out-of-plane direction and 2.0 nm along the in-plane direction. Annealing at 400 °C for 10 min in air induces densifications in both TiO_2 and Al_2O_3 layers, which could be due to the initiated crystallization in the TiO_2 layer and the shrinking of pores and loss of hydrogen from hydroxyl groups in the Al_2O_3 layer. Annealing at 400 °C for 40 min in air can eliminate pores in the Al_2O_3 layer which could account for the slight densification after annealing for the longer time besides the hydrogen loss. Non-porous Al_2O_3 is also obtained with varying ALD parameters, which is accompanied by increased density and refractive index of the Al_2O_3 layer.

The multilayer $Al_2O_3/TiO_2/Al_2O_3$ ARC on Si has amorphous structures. The ARC layers are flat parallel to the substrate and have surface and interface roughness and/or grading on the order of 1 nm. Annealing at 400 °C for 10 min in air induces densification of the TiO_2 layer which could be due to the initiation of crystallization and the possible chemical reaction between TiO_2 and the Si diffusing from the substrate. On the other hand, Al_2O_3 layers remain amorphous after annealing. The thickness of the top Al_2O_3 layer decreases which is likely due to interdiffusion of Al and Ti between the top two ARC layers and the loss of hydrogen from hydroxyl groups. The thickness of the bottom Al_2O_3 layer increases which could be attributed to the diffusion of Si atoms into the bottom layer.

The multilayer $Al_2O_3/TiO_2/Al_2O_3$ ARC is also deposited on an AlInP (30 nm) / GaInP (100 nm) / GaAs substrate with flat layers parallel to the substrate and small surface and interface roughnesses and/or grading less than 1 nm. Initiated crystallization occurs in the TiO_2 layer while Al_2O_3 layers are amorphous. The multilayer ARC achieves broadband low reflectance less than 5 % within 450 – 810 nm which is nearly the whole range of the current limiting sub-cell in IMM4JSC and a minimum of ~ 2 % throughout 550 – 750 nm. On the other hand, internal scattering in the multilayer $Al_2O_3/TiO_2/Al_2O_3$ ARC within 400 – 800 nm is revealed. This originates from the TiO_2 layer probably due to the initiated crystallization. It could be a combination of Rayleigh scattering from the small grains (size < ~ 35 nm) and Mie scattering from the large grains (size > ~ 35 nm).

8.2   Future Work

ARCs deposited by ALD have ~ 90 % and ~ 75 % of bulk densities for TiO_2 and Al_2O_3, respectively. Post-annealing and varying ALD parameters both change layer

thicknesses, densities, and refractive indices. Although pore size distribution and crystal structures of the ARC layers were characterized in this study, it is also necessary to characterize non-stoichiometry and hydroxyl groups that are associated with densities and refractive indices as well in order to fully understand how optical properties are influenced by the optimization methods. Also, studies on influences of more deposition and annealing conditions would provide more comprehensive information for ARC optimization.

Post-annealing and varying deposition parameters enable to yield either porous or non-porous films. They would serve as effective approaches in tuning optical, electrical and mechanical properties of thin films through varying porosities and pore sizes. In the meantime, it is important to keep pore sizes within the acceptable ranges for different applications. The combined approach of GISAXS, AFM, and XRR developed in this study provides a useful tool that accurately characterizes pore size distribution in thin films. It effectively revealed the difference in pore scattering even for the films with similar densities (less than 3 % difference). Applications of this approach include any thin films with surface roughness below ~ 5 nm and density difference between the layer and the substrate above ~ 10 %. Therefore, this combined approach of GISAXS, AFM, and XRR can be applied to many other research areas, which also helps validate this approach.

Bibliography

1. L. Rayleigh, Proc. London Math. Soc. **s1-11,** 51 (1879).

2. K.Citek, Optometry **79,** 143 (2008).

3. N. Oda, M. Sano, K. Sonoda, H. Yoneyama, S. Kurashina, M. Miyoshi, T. Sasaki, I. Hosako, N. Sekine, T. Sudou, and S. Ohkubo, Proc. SPIE **8012,** 80121B (2011).

4. D. Swetz, P. Ade, C. Allen, M. Amiri, J. Appel, E. Battistelli, B. Burger, J. Chervenak, A. Dahlen, S. Das, et al., Proc. SPIE **7020,** 702008 (2008).

5. S. Chhajed, M. F. Schubert, J. K. Kim, and E. F. Schubert, Appl. Phys. Lett. **93,** 251108 (2008).

6. O. S. Heavens, *Optical Properties of Thin Solid Films* (Dover, New York, 1991).

7. F. Dimroth, T. N. D. Tibbits, M. Niemeyer, F. Predan, P. Beutel, C. Karcher, E. Oliva, G. Siefer, D. Lackner, P. Fus-Kailuweit, A. W. Bett, R. Krause, C. Drazek, E. Guiot, J. Wasselin, A. Tauzin, and T. Signamarcheix, IEEE J. Photovoltaics **6,** 343 (2016).

8. M. Stan, D. Aiken, B. Cho, A. Cornfeld, J. Diaz, A. Korostyshevsky, V. Ley, P. Patel, P. Sharps, and T. Varghese, Proc. 33th IEEE PVSC 1 (2008).

9. D.C. Law, X.Q. Liu, J.C. Boisvert, E.M. Redher, C.M. Fetzer, S. Mesropian, R.R. King, K.M. Edmondson, B. Jun, R.L. Woo, D.D. Krut, P.T. Chiu, D.M. Bhusari, S.K. Sharma, N.H. Karam, Proc. 38th IEEE PVSC 3146 (2012).

10. P.T. Chiu, D.C Law, R.L. Woo, S.B. Singer, D. Bhusari, W.D. Hong, A. Zakaria, 1. Boisvert, S. Mesropian, R.R. King, and N.H. Karam, Proc. 40th IEEE PVSC 11 (2014).

11. P. T. Chiu, D. C Law, S. B. Singer, D. Bhusari, A. Zakaria, X. Q. Liu, S. Mesropian, and N. H. Karam, Proc. 42th IEEE PVSC 1 (2015).

12. R. R. King, A. Boca, W. Hong, X.-Q. Liu, D. Bhusari, D. Larrabee, K. M. Edmondson, D. C. Law, C. M. Fetzer, S. Mesropian, and N. H. Karam, Bad-Gap-Engineered Architectures for High-Efficiency Multijunction Concentrator Solar Cells, 24th European Photovoltaic Solar Energy Conference and Exhibition WIP Renewable Energies, Hamburg, Germany, 2009.

13. G. S. Kinsey and K. M. Edmondson, Prog. Photovoltaics **17,** 279 (2009).

14. C. E. Valdivia, E. Desfonds, D. Masson, S. Fafard, A. Carlson, J. Cook, T. J. Hall, and K. Hinzer, Proc. SPIE **7099,** 709915 (2008).

15. J. Zhao and M. A. Green, IEEE Trans. Electron Devices **38,** 1925 (1991).

16. W.J. Aziz, A. Ramizy, K. Ibrahim, Z. Hassan, K. Omar, The effect of antireflection coating of porous silicon on solar cells efficiency, OPTIK. Int. J. Light Electron Opt. **122,** 1462 (2011).

17. R. Homier, A. Jaouad, A. Turala, C. E. Valdivia, D. Masson, S. G. Wallace, S. Fafard, R. Ares, and V. Aimez, IEEE J. Photovoltaics **2,** 393 (2012).

18. G. Triani, P. J. Evans, D. R. Mitchell, D. J. Attard, K. S. Finnie, M. James, and J. Bartlett, Proc. SPIE. **5870,** 587009 (2005).

19. N. B. Abaffy, D. G. McCulloch, J. G. Partridge, P. J. Evans, and G. Triani, J. Appl. Phys. **110,** 123514 (2011).

20. D. J. Aiken, Sol. Energy Mater. Sol. Cells. **64,** 393 (2000).

21. L. I. Epstein, J. Opt. Sot. Am. **42,** 806 (1952).

22. U. B. Schallenberg, Appl. Opt. **45,** 1507 (2006).

23. T. Suntola, Mater. Sci. Rep. **4,** 261 (1989).

24. I. D. Scott, Y. S. Jung, A. S. Cavanagh, Y. Yan, A. C. Dillon, S. M. George, and S.-H. Lee, Nano Lett. **11,** 414 (2011).

25. E. M. Lotfabad, P. Kalisvaart, A. Kohandehghan, K. Cui, M. Kupsta, B. Farbod and D. Mitlin, J. Mater. Chem. A **2,** 2504 (2014).

26. R. Singh, R. Bapat, L. Qin, H. Feng and V. Polshettiwar, ACS Catal. **6,** 2770 (2016).

27. K. M. H. Young and T. W. Hamann, Chem. Commun. **50,** 8727 (2014).

28. A. B. Sachid, M. Tosun, S. B. Desai, C.-Y. Hsu, D.-H. Lien, S. R. Madhvapathy, Y.-Z. Chen, M. Hettick, J. Seuk Kang, Y. Zeng, J.-H. He, E. Yi Chang, Y.-L. Chueh, A. Javey and C. Hu, Adv. Mater. **28,** 2547 (2016).

29. P. F. Carcia, R. S. McLean, and M. H. Reilly, Appl. Phys. Lett. **88,** 123509 (2006).

30. N. Bilus Abaffy, P. Evans, G. Triani, and D. McCulloch, Proc. Soc. PhotoOpt. Instrum. Eng. **7041,** 704109 (2008).

31. Z. Li, S. T. Barry, and R. G. Gordon, Inorg. Chem. **44,** 1728 (2005).

32. S. H. Kim, E. S. Hwang, B. M. Kim, J. W. Lee, H. J. Sun, T. E. Hong, J. K. Kim, H. Sohn, J. Kim, and T. S. Yoon, Electrochem. Solid-State Lett. **8,** C155 (2005).

33. S. Sinha, D. Choudhury, G. Rajaraman, and S. K. Sarkar, RSC Adv. **5,** 22712 (2015).

34. N. P. Dasgupta, X. Meng, J. W. Elam, A. B. F. Martinson, Acc. Chem. Res. **48,** 341 (2015).

35. T. Dobbelaere, M. Minjauw, T. Ahmad, P. M. Vereecken, and C. Detavernier, J. Non-Cryst. Solids **444,** 43 (2016).

36. J. Hamalainen, J. Holopainen, F. Munnik, M. Heikkila, M. Ritala and M. Leskela, J. Phys. Chem. C **116,** 5920 (2012).

37. M. D. Groner, F. H. Fabreguette, J. W. Elam, and S. M. George, Chem. Mater. **16,** 639 (2004).

38. G. Dingemans, M. C. M. van de Sanden, and W. M. M. Kessels, Electrochem. Solid-State Lett. **13,** H76 (2010).

39. J. L. van Hemmen, S. B. S. Heil, J. Klootwijk, F. Roozeboom, C. J. Hodson, M. C. M. van de Sanden, and W. M. M. Kessels, J. Electrochem. Soc. **154,** G165 (2007).

40. Y. Liu, A. R. Oganov, S. Wang, Q. Zhu, X. Dong, G. Kresse, Sci. Rep. **5,** 9518 (2015).

41. V. Miikkulainen, M. Leskelau, M. Ritala, and R. L. Puurunen, J. Appl. Phys. **113,** 021301 (2013).

42. Y. Q. Hou, D. M. Zhuang, G. Zhang, M. Zhao, and M. S. Wu, Appl. Surf. Sci. **218,** 97 (2003).

43. V. Gupta and A. Mansingh, J. Appl. Phys. **80,** 1063 (1996).

44. F. Zhang, W. Yang, A. Pang, Z. Wu, H. Qi, J. Yao, Z. Fan, and J. Shao, Appl. Surf. Sci. **254,** 6410 (2008).

45. A. C. Dillon, A. W. Ott, J. D. Way, and S. M. George, Surf. Sci. **322,** 230 (1995).

46. V. Verlaan, L. R. J. G. van den Elzen, G. Dingemans, M. C. M. van de Sanden, and W. M. M. Kessels, Phys. Status Solidi C **7,** 976 (2010).

47. A. Szeghalmi, M. Helgert, R. Brunner, F. Heyroth, U. G€osele, and M. Knez, Appl. Opt. **48,** 1727 (2009).

48. D. Franta, I. Ohlídal, and D. Petrýdes, Vacuum **80,** 159 (2005).

49. B. Poust, R. Sandhu, and M. Goorsky, Phys. Status Solidi A. **206,** 1780 (2009).

50. D. R. G. Mitchell, G. Triani, D. J. Attard, K. S. Finnie, P. J. Evans, C. J. Barbé, and J. R. Bartlett, Smart Mater. Struct. **15,** S57 (2006).

51. O. Glatter and O. Kratky, *Small Angle X-ray Scattering* (Academic, New York, 1982).

52. K. Omote, Y. Ito, and S. Kawamura, Appl. Phys. Lett. **82,** 544 (2003).

53. T. Suzuki, K. Omote, Y. Ito, I. Hirosawa, Y. Nakata, I. Sugiura, N. Shimizu, and T. Nakamura, Thin Solid Films **515,** 2410 (2006).

54. M. Wormington and C. Russell, Proc. AIP Conf. **683,** 651 (2003).

55. L. G. Parratt, Phys. Rev. **95,** 359 (1954).

56. Nevot, L. and P. Croce, Rev. Phys. Appl. **15,** 761 (1980).

57. M. Wormington, C. Panaccione, K. M. Matney, and D. K. Bowen, Philos. Trans. R. Soc. London, Ser. A **357,** 2827 (1999).

58. O. Durand, Thin Solid Films **450,** 51 (2004).

59. I. K. Robinson, Phys. Rev. B **33,** 3830 (1986).

60. S. Banerjee, G. Raghavan, and M. K. Sanyal, J. Appl. Phys. **85,** 7135 (1999).

61. L. Grave de Peralta and H. Temkin, Appl. Phys. Lett. **93,** 1974 (2003).

62. G. N. Greaves, M. C. Wilding, S. Fearn, D. Langstaff, F. Kargl, S. Cox, Q. Vu Van, O. Majerus, C. J. Benmore, R. Weber, C. M. Martin, and L. Hennet, Science **322,** 566 (2008).

63. G. N. I. Clark, G. L. Hura, J. Teixeira, A. K. Soper, and T. Head-Gordon, Proc. Natl. Acad. Sci. U.S.A. **107,** 14003 (2010).

64. J. Lee, S. Jin, Y. Hwang, J. Park, H. Park, and T. Hyeon, Carbon, **43,** 2536 (2005).

65. M. Rauscher, T. Salditt, and H. Spohn, Phys. Rev. B **52,** 16855 (1995).

66. H. Dosch, *Critical Phenomena at Surfaces and Interfaces* (Springer, Berlin, 1992).

67. J. R. Levine, J. B. Cohen, Y. W. Chung, and P. Georgopoulos, J. Appl. Crystallogr. **22,** 528 (1989).

68. M. L. Green, A. J. Allen, J. L. Jordan-Sweet, and J. Ilavsky, J. Appl. Phys. **105,** 103522 (2009).

69. V. Chamard, P. Bastie, D. Le. Bolloch, G. Dolino, E. Elkaïm, C. Ferrero, J.-P. Lauriat, F. Rieutord, and D. Thiaudière, Phys. Rev. B **64,** 245416 (2001).

70. M. Buljan, N. Radic, S. Bernstorff, G. Drazic, I. Bogdanovic-Radovic and V. Holy, Acta Cryst. **A68,** 124 (2012).

71. P. P. Ewald, Phys Z **14,** 465 (1913).

72. S. Dietrich and A. Haase, Phys. Rep. **260,** 1 (1995).

73. S. K. Sinha, E.B. Sirota, S. Garoff, and H.B. Stanley, Phys. Rev. B **38,** 2297 (1988).

74. D. Necas, and P. Klapetek, Cent. Eur. J. Phys. **10,** 181 (2012).

75. S. Forster, L. Apostol and W. Bras, J. Appl. Cryst. **43,** 639 (2010).

76. O. Anderson, C. R. Ottermann, R. Kuschnereit, P. Hess, and K. Bange, Fresenius. J. Anal. Chem. **358,** 315 (1997).

77. M. Cho, H. B. Park, J. Park, C. S. Hwang, J. C. Lee, S. J. Oh, J. Jeong, and K. S. Hyun, J. Appl. Phys. **94,** 2563 (2003).

78. G. D. Wilk, R. M. Wallace, and J. M. Anthony, J. Appl. Phys. **89,** 5243 (2001).